Characterization of Oligo-Miocene evaporite-rich minibasins in the Sivas Basin, Turkey

Alexandre Pichat, Guilhem Hoareau, Jean-Paul Callot, Jean-Claude Ringenbach

Characterization of Oligo-Miocene evaporite-rich minibasins in the Sivas Basin, Turkey

Alexandre Pichat (1, 2), Guilhem Hoareau (1), Jean-Paul Callot (1), Jean-Claude Ringenbach (2).

(1) E2S-UPPA, Total, CNRS, Univ. Pau & Pays Adour, Laboratoire des Fluides Complexes et leurs Réservoirs-IPRA, UMR5150; 64013, Pau, France

(2) Total SA, CSTJF, avenue Larribau, 64018 Pau, France

Corresponding author: Alexandre Pichat, alexandre.pichat@gmail.com

Abstract

The Sivas Basin in Turkey displays in its central part an Oligo-Miocene halokinetic province which acts as a major outcrop analogue to study salt-sediment interactions. Based on field geology observations, the present paper focuses on the geometry and sedimentology of several minibasins having the particularity of being mainly filled by gypsiferous deposits. Such type of evaporite-rich minibasins remain difficult to identify and are poorly studied in other halokinetic provinces. In the Sivas Basin, the evaporites were recycled from diapiric salts and precipitated in saline ponds emplaced above deflating diapiric stems. Diapir deflation resulted either from local transtensive strain, cessation of diapir feeding and / or subsurface dissolution of the diapiric salt. Minibasin subsidence was likely enhanced by the fast emplacement rate of the capping evaporites, together with the high density of the depositional sulfates compared to the diapiric halite. The evaporite-rich minibasins stand out from their surrounding siliciclastic counter-parts by their small dimension (lower than 1 km-wide), their encased teardrop shape, and their high internal deformations. The later include well-developed halokinetic sedimentary wedges, aerial mega-slumps or inverted flaps. Such structural features probably resulted from the ductile rheology of the evaporite infill and the complex pattern of downbuilding. Although secondary evaporitic minibasins have never been identified in other ancient halokinetic settings, our study highlights that they could developed in any evaporitic environments, coastal or continental, such as in the Precaspian Basin. The secondary minibasins described here can also act as field analogues of other primary evaporite-rich minibasins already suspected in salt giant basins (e.g. in the Brazilian margin).

Keywords: Sivas Basin, salt tectonics, secondary minibasin, gypsum, anhydrite, evaporite recycling.

I. Introduction

Salt-related minibasins are restricted depocenters subsiding into thick salt accumulations (Callot et al., 2016; Hudec et al., 2009; Hudec and Jackson, 2007). In several halokinetic provinces, minibasins filled with marine to continental siliciclastic and carbonate deposits have been described and investigated in terms of salt-sediment interactions (e.g. Banham and Mountney, 2013a; Madof et al., 2009; Oluboyo et al., 2014; Poprawski et al., 2016; Ribes et al., 2016; Rowan et al., 2003). However, they are only a limited amount of work that focused on minibasins mostly filled by evaporitic facies. On outcrop, they have only been succinctly described in the Sivas Basin in Turkey (Collon et al., 2016; Ribes et al., 2016) and reported in recent deposits of the Precaspian basin (Barde et al., 2002; Belenitskaya, 2018). In subsurface, evaporite-rich minibasins have been confirmed by wells penetrating several of them in the Precaspian Basin (Fernandez et al., 2017; Jackson et al., 2013). Elsewhere, due to limited seismic resolution and lack of well-penetrations in thick salt accumulations, evaporite-rich minibasins have just been inferred, as in the case of the Brazilian passive margin (Davison et al., 2012; Gamboa et al., 2008; Quirk et al., 2012) and of the North Sea (Clark et al., 1998; Stewart and Clark, 1999). The existence of intra-salt evaporitic minibasin is especially debated in the Santos basin (Brazil), with publications highlighting that intra-salt geometries may result from post-depositional deformations rather than from syn-depositional salt-infilled minibasin subsidence (Dooley et al., 2015b; Jackson et al., 2015). To sum-up, evaporite-rich minibasins remain poorly understood and their tectono-sedimentary peculiarities still need to be constrained.

However, minibasins filled by evaporite facies may play an important role in the salt-tectonic related evolution of major oil provinces. First, evaporitic rocks display three properties that distinguish them from other sedimentary deposits, and that are directly related to salt tectonics: they have among (i) the fastest sedimentation rates (commonly ~ 5 cm/year for halite and ~ 1 cm/year for gypsum; Warren, 2016), (ii) the weakest rheologies (evaporites are 50 to 100 times less viscous than other sedimentary rocks; Davison et al., 1996; Warren, 2016), and (iii) the highest densities along the first 1000 m of burial (Fernandez et al., 2017; Hudec et al., 2009; especially for anhydrite, van den Belt and de Boer, 2007). Accordingly, specific salt-sediment interactions and/or structural features may be expected in evaporitic minibasins, and their description could significantly improve the analysis of seismic data during processing. Second, an entire petroleum system might be present interbedded with thick evaporite accumulations because (i) evaporitic environments are prone to the accumulation of organic-rich sediments (Warren, 2011), (ii) evaporites have good sealing capacities and (iii) evaporite facies can be interlayered with porous sediments (e.g. Al-siyabi, 2005). This explains why the intra-salt Permian sediment packages in the Precaspian Basin, and related evaporite-rich minibasins, are relevant targets for hydrocarbon exploration (Fernandez et al., 2017). Accordingly, the identification and understanding of evaporite-rich minibasins may ground the discovery of new oil resources.

The Sivas Basin in Turkey displays outcrop conditions that enable a better description of the sedimentary infill and small-scale geometries of evaporite-rich minibasins (EMBs). This foreland basin shows well-exposed km-scale minibasins, bordered by diapiric evaporites and filled with continental to marine siliciclastic sediment packages and/or gypsiferous deposits which have been recycled from nearby diapiric structures (Callot et al., 2014; Çubuk and Inan, 1998; Kergaravat et al., 2017, 2016; Legeay et al., 2019b; Pichat et al., 2018, 2016; Ribes et al., 2018, 2016, 2015; Ringenbach et al., 2013). In the central halokinetic domain, four minibasins mostly filled by evaporite facies, have been previously identified with limited lithological description of the sedimentary infill (Kergaravat et al., 2017; Ribes et al., 2016). In the course of this study, four additional ones with singular geometries have been studied through detailed field-mapping.

On the basis of field-work and thin-sections inspection, the present study (i) outlines and characterizes the EMBs encountered in the Sivas Basin, in terms of sedimentology and geometry, (ii) highlights their specificities compared to other non-evaporitic minibasins, and (iii) discusses the mechanisms controlling their formation and evolution.

II. Geological setting

The Sivas basin is located in the centre-east of Turkey (Fig. 1). It developed above three crustal blocks: the Pontides arc to the north, the Tauride–Anatolide to the south, and the Kirşehir block to the west (Cater et al., 1991; Yilmaz and Yilmaz, 2006). The basin is a foreland that initiated in the late Cretaceous, during the collision of the three crustal blocks, and after the obduction of ophiolitic materials of the Neotethys Ocean (Cater et al., 1991; Dilek and Sandvol, 2009; Görür et al., 1998; Gürer et al., 2016; Kergaravat et al., 2016; Legeay et al., 2019c, 2019a; Meijers et al., 2010; Okay et al., 2006; Poisson et al., 1996; Robertson et al., 2012; Rolland et al., 2010; Yilmaz and Yilmaz, 2006).

From the Maastrichtian to the Late Eocene, the sedimentation was mainly characterized by marine limestones (Teçer and Gürlevik Formations), alluvial to deltaic clastics (Bahçecik Formation) and deepwater volcanoclastics and turbidites (Çerpaçindere, Kozcula, Yapali and Bözbel Formations) (Fig. 2) (Aktimur et al., 1990; Altunsoy and Özçelik, 1998; Artan and Sestini, 1971; Cater et al., 1991; Kurtman, 1973; Legeay et al., 2019a; Poisson et al., 2010).

The Late Eocene records the closure of the foreland from the marine domain, and a transition from clastic and carbonate deposition to evaporite deposits (Tuzhisar Formation) (Kurtman, 1973; Özçelik and Altunsoy, 1996; Tekin, 2001; Yilmaz and Yilmaz, 2006). It was estimated that about 2 km of evaporites precipitated during this period (Kergaravat et al., 2016; Legeay et al., 2019c) in a marine-fed foredeep (Pichat, 2017).

In the central part of the basin, these evaporites controlled the development of two generations of salt-walled minibasins during the Oligocene and the Miocene (Callot et al., 2014; Kergaravat et al., 2017, 2016; Legeay et al., 2019b; Ribes et al., 2016, 2015; Ringenbach et al., 2013). The first generation of minibasins was filled by fluvial deposits (Selimiye Formation) and they were separated by emerging diapirs and walls (Kergaravat et al., 2016; Ribes et al., 2016). The second generation of minibasins developed above a large salt canopy fed by the former evaporite diapirs (Fig. 2; Kergaravat et al., 2016). These secondary minibasins were filled by three successive sedimentary formations: the Karayün, the Karacaören and the Benlikaya formations (Callot et al., 2014; Kergaravat, 2016; Ribes et al., 2018, 2016). The late Oligocene Karayün Formation corresponds to a distributary fluvial system and is subdivided into three units associated to playa-lake (Unit 1), fluvial (Unit 2) and lacustrine to sabkha environments (Unit 3) (Ribes et al., 2016). The early Miocene Karacaören Formation records a transgressive event and includes shallow water marine limestones, sandstones and marls (Ribes et al., 2018). The middle Miocene Benlikaya Formation is continental and also characterizes a distributive fluvial system. It is subdivided in two units: Unit 1 is marked by coarse-grained alluvial to fluvial deposits, whereas Unit 2 displays fine-grained deposits and evaporitic facies (Ribes et al., 2018).

At present, the Oligo-Miocene minibasins outcrop in the central part of the Sivas Basin within a wall and basin province (Fig. 2) (Kergaravat et al., 2017, 2016; Legeay et al., 2019b, 2019c). They are surrounded by diapiric evaporites made up of chaotic accumulations of residual sulphates (anhydrite and gypsum left after the dissolution of halite) more or less sheared and mixed with red to green clays (Pichat, 2017). Previous sedimentological studies highlighted that semi-arid conditions regularly triggered evaporitic deposition during the Oligo-Miocene (Çiner et al., 2002; Ocakoğlu et al., 2017; Pichat et al., 2016; Ribes, 2015; Ribes et al., 2016). Within the minibasins, significant evaporite-rich accumulations (up to 600 meters-thick) especially occurred (i) in the Upper member of the Karayün Formation, interlayered with lacustrine and sheet flood deposits, and (ii) in the Unit 2 of the Benlikaya Formation, interlayered with playa-lake deposits (Fig. 2, Ribes *et al.*, 2016; Pichat, 2017; Ribes *et al.*, 2018). Such deposits were favored by periods of low sediment supply and / or high accommodation regime linked to the flexural subsidence of the basin during the growth of the southern orogenic belt (Ribes et al., 2018, 2016). Finally, the dissolved elements feeding the evaporites were mostly provided by the meteoric leaching of the outcropping diapiric structures (i.e. recycled evaporites), with the local influence of marine-water in the Upper Member of the Karayün Formation (Pichat et al., 2018).

III. Data and methods

Fieldwork investigations in the studied area (Fig. 2 A) were based on the 1/10,000 geological map compiled by Legeay *et al.* (2018) with the help of Google Earth satellite images. The 8 evaporites-bearing minibasins presented on fig. 2 A, and covering ~9.5 km^2, were first studied on satellite images (0.5 m resolution) and then studied on field outcrop for sedimentological and structural analysis. Due to outcrop conditions, the Inceyöl minibasin is the only one in which the sedimentary infill (~330 m) could be entirely logged and detailed. Facies analyses were complemented by petrographical observations made on 11 polished thin sections. Cross sections are based on the surface data and were built by using a digital elevation models with a resolution of 2m x 2m. Sub-surface interpretations of the cross-sections are based on geometrical assumptions in accordance with (i) the faults, fold and strata surface measurements, (ii) the panoramic observations, (iii) the structural model of the Sivas Basin published by Kergaravat et al., (2016), Kergaravat et al. (2017), Legeay (2017) and Legeay et al. (2018) and (iv) the geometrical analysis from published subsurface data in other salt dominated provinces (e.g. Barde et al., 2002; Fernandez et al., 2017; Giles and Rowan, 2012; Hudec and Jackson, 2017)).

IV. Characterization of evaporite-rich minibasins

A. General description

a. Location

In addition to the four EMBs previously highlighted in other studies (namely Pınarca, Köy, Inceyol and Ulukapı; Collon *et al.*, 2016; Ribes *et al.*, 2016; Kergaravat *et al.*, 2017), four other EMBs have been identified within the central halokinetic domain of the Sivas Basin (Koyuncu, Devrik, Cekmis and Damla) (Fig. 2 A). These basins lie directly above allochthonous evaporites and are surrounded by other continental to marine minibasins. The EMBs may locally be in contact with the surrounding siliciclastic minibasins, without any clear diapiric wall separating both minibasins. But these contacts often display shale-rich sinuous surfaces presenting isolated meter-wide patches of gypsum, associated with evidence of halokinetic structures along the contacts (e.g. halokinetic wedge or hooks). These contacts are thus interpreted as welds on map (e.g. the eastern border of the Köy minibasin, see Kergaravat et al., 2017). The Cekmis minibasin displays a southern border which is rather interpreted as a normal fault plane probably deeply rooted in the allochthonous evaporite sheet: the contact with the southern Oligo-Miocene deposits is straight, there are no remnant patches of diapiric evaporites along the surface and there is no evidence of halokinetic structures on either sides of the contact.

b. Age

The Köy minibasin is the only one to have been dated from the Chattian (included in the Unit 3 of the Karayün Formation) based on charophyte fossils ocurrences (Poisson et al., 2012). Relative-age dating was used for the other EMBs, considering the age of the continental to marine formations in the nearby siliciclastic minibasins and the fact that the EMBs were most probably filled during evaporite-rich periods of the Oligo-Miocene. Accordingly, depending of its localization, we infer that some EMBs were completely filled during the deposition of Unit 3 of the Karayün Formation whereas other were filled during the Unit 2 of the Benlikaya Formation (Fig. 2 A). However, since absolute dating is lacking and since arid conditions were always favoring evaporite deposition during the Oligo-Miocene period (Ribes et al, 2016, 2018), we cannot exclude that some EMBs represent depocenters which formed during siliciclastic-rich periods (e.g. during the Unit 1 of the Benlikaya Formation) if they were isolated from the fluvial-inputs having fed the wider minibasins (Banham and Mountney, 2013a).

c. Sedimentary infill

Measured or estimated sedimentary thickness in the EMBs ranges from a few hundred meters to more than one thousand meters (e.g. Ribes et al., 2016). In the EMBs of Koyuncu, Cekmis and Damla, the sediments are only made up of regular alternation of gypsiferous beds and green to grey clays. In the other EMBs, up to 60 % of the sedimentary infill also records stratigraphic intervals characterized by red to green clays and pelites interlayered with isolated carbonate and sandstone beds. This type of bimodal sedimentary infill is illustrated on figure 3 with the 330 meter-thick sedimentary section of the Inceyol minibasin, in which the lower half part of the basin is mostly gypsum-free, whereas the upper half part displays 8 evaporitic units, 2.5 to 15 meters-thick interlayered with mud-rich gyspiferous intervals.

The facies and related depositional environments of the EMB are further described below.

d. Geometry

Some of the EMBs display a sub-circular to elliptical shape cored by a central syncline (*e.g.* the Devrik and Koyuncun minibasins). Other EMBs bounded by welds and faults display a rather polygonal shape with three or more, usually straight, sides (e.g. Pinarca and Cekmis minibasins).

The EMBs are characterized by their small dimension compared to other siliciclastic minibasins. The largest EMB is the Devrik minibasin, with a width of ~1.7 km and a length of ~2 km (Fig. 2 A). Other EMBs can be less than 1 km wide (*e.g.* the Inceyol minibasin, 0.5 km width). As a result, at the map scale, the EMBs cover areas lower than 2 km^2 whereas other non-evaporitic minibasins cover areas commonly comprised between 5 and 60 km^2 (Fig. 2 A).

e. Origin

The small-size of the EMBs, their confinement between wider and older siliciclastic minibasins, their lack of siliciclastic-rich deposits and the upper Oligocene age of the only EMB dated, altogether suggest that the EMBs are not primary but rather secondary, as previously proposed by Ribes et al. (2016) and Kergaravat et al. (2017). In other word, the EMBs formed as isolated minibasins having sunk into allochtonous salt-walls or diapirs (e.g. Hodgson et al., 1992; Hudec, 1992; Hudec et al., 2009; Vendeville and Jackson, 1992).

B. Facies associations and related depositional environments of the evaporitic minibasins

The EMB are dominated by5 major facies associations (FAs): siliciclastic and carbonate deposits (FA1) laminated-banded gypsum (FA 2), enterolitic to nodular-banded gypsum (FA 3), selenitic gypsum (FA 4) and massive secondary gypsum (FA 5). In lower proportion, two other FAs are observed: nodular gypsum (FA 6) and siliciclastic-rich gypsum (FA 7). Each FA are hereafter described in interpreted, together with a last, specific, facies composed of post-depositional breccia.

a. Facies association 1: Siliciclastic and carbonate deposits

Description: This facies association is characterized by fissile red pelites and green to grey shales enclosing thin beige carbonate beds and greenish sandstone bodies (Fig. 3). Carbonate beds forms bioclastic packstones that are centimeter to decimeter-thick, and rich in charophyte fragments, shells and molds of ostracodes and gastropods (Fig. 3 C and D). The sandstones beds are medium to fine-grained, centimeter to 1.5 meter-thick, and tabular to channelized over tens of meters. They locally display lag deposits, are commonly slightly normally graded with parallel to cross stratifications and wave ripples (Fig. 3 E).

Interpretation: The red clays are interpreted as having been deposited in alluvial plain environments whereas the green clays probably laterally settled in perennial and / or ephemeral lakes. In such environments, the isolated sandstone bodies record occasional flood events (Ribes et al., 2016). According to their fossil content, the carbonate beds accumulated in shallow-water brackish condition (Ribes et al., 2016), most probably over the margin of the former lake, where wave ripples could also develop atop the sandstone bodies.

b. Facies association 2: Laminated-banded gypsum

Description: FA 2 displays regular and thin alternations of millimeter- to few centimeter-thick beds of microcrystalline gypsum (composing 50% to 70% of the FA) and green to dark clays variably cemented by gypsum (Fig. 4 F, G). The gypsum layers are either continuous with a relatively constant thickness, sometimes discontinuous and lenticular. They are usually wavy, contorted or with crenulated structures (Fig. 4 F, G). The discontinuous gypsum layers display centimeter bowl-shaped structures (Fig. 4 F). Thickest gypsum layers (~2 cm) are commonly the most continuous and crenulated. Some of these layers show tepee-like structures (Fig. 4 G). Finally, small (mm-thick) gypsum micronodules interlayered in the muddy intervals are frequent (Fig. 4 F).

Interpretation: The finest gypsum laminae interlayered with clays probably record former cumulates, precipitated at the air-water interface in a saline lake (Magee, 1991). The contorted aspect of the laminae may result from (i) soft sediment deformations due to diagenetic transformations (i.e anhydritisation of gypsum during burial and re-hydration of anhydrite into gypsum during exhumation, Shearman, 1978; Hussain and Warren, 1989), (ii) algal mat growth at the sediment surface (e.g. Castens-Seidell, 1984) or (iii) reworking of the gypsum crystals by wave current (e.g. Logan, 1987). The thickest and more continuous gypsum layers probably record former thin gypsum crusts precipitated at the sediment-water interface of the saline lake (Arakel, 1980; Castens-Seidell, 1984; Hardie and Eugster, 1971). Their crenulated top would outline the crystalline shape of the former gypsum crystals, now erased by diagenetic transformations (e.g. Kirkham, 2011). The discontinuous or lensoidal gypsum layers fit with thin gypsum crust precipitated by efflorescence at the sediment-air interface in dry seasons (e.g. Bobst et al., 2001). The bowl-shaped structures of these layers, or the tepee-like shapes in the thickest beds, are interpreted as desiccation cracks that evidence desiccation events of the saline pond. Such events could have favored the early anhydritisation of the gypsum beds (erasing the primary gypsum textures) and the precipitation of the tiny gypsum nodules, through evaporitic pumping (e.g. Hussain and Warren, 1989; Kirkham, 2011). Alternatively, the bowl like structures may have resulted from early dewatering process during shallow burial. Finally, before settling in the lake, the clayey deposits were likely brought by (i) fluvial inputs during more humid periods, and /or (ii) by the wind (Aref et al., 1997; e.g. Castens-Seidell, 1984; Raup and Hite, 1992).

Accordingly, this FA is interpreted as characterizing a shallow and gypsum-saturated lacustrine environment (saline pond) that was subjected to seasonal salinity fluctuations and occasional desiccation periods associated to limited sabkhatisation processes (Aref et al., 1997; Hussain and Warren, 1989; López-Quirós et al., 2018; Magee, 1991).

c. Facies association 3: Enterolithic to nodular banded gypsum

Description: FA 3 is made up of centimeter to decimeter-thick enterolithic to nodular continuous gypsum beds thinly interlayered with green clays composing ~40% of the FA (Fig. 4 H, I). The nodules are frequently vertically oriented resulting in a crenulated top of the gypsum beds (Fig. 4 I). Scarce flat and discrete erosive surfaces are locally observed above dome-like shapes up to 10 cm-high and 15 cm-wide and formed by highly contorted entherolitic gypsum layers (Fig. 4 H).

Interpretation: The lateral continuity of the gypsum beds, the well bedded aspect and the vertical elongations of the gypsum nodules all together suggest that the gypsum layers record former accumulations of bottom-growth gypsum crusts having been intensively diagenetised during burial and exhumation (dehydration and rehydration; Hussain and Warren, 1989; Shearman, 1978). The related recrystallization processes are responsible for the enterolitic structures (Kirkham, 2011). The dome-like shapes probably formed through competitive growth of the former selenite crystals (Hardie and Eugster, 1971; Warren, 1982) whereas the capping erosive surfaces result from desiccation events, or possibly mark dissolution surfaces due to dilution events (e.g. Bąbel, 2007; Warren, 1982). The latter were induced by recurrent flooding having periodically brought the mud layers, above which new generations of gypsum crystals successively grew.

d. Facies association 4: Thick selenitic gypsum

Description: FA 4 is characterized by crystalline gypsum of selenitic habit forming continuous and well-stratified centimeter- to meter-thick beds interlayered with thin (< 1 cm) mud to calcite layers constituting less than 10% of the FA (Fig. 5 A, B). Crystals can be few millimeters to 4 centimeters long (average ~1.5 cm). They are single or twined along the (100) plane (swallow-tail twin). In some layers, the crystals are preferentially vertically oriented and may form beds displaying crenulated to domal structures (Fig. 5 A, B). In some other layers, the crystals are un-oriented and embedded in a muddy and micritic matrix (Fig. 5 C, D). Such strata can also display current ripples (Fig. 5 E). Finally, thin strata display anhydritisation features (whitening of the crystals or small anhydrite nodules; Fig. 5 A).

Interpretation: These crystalline facies characterize a perennial shallow saline pan that allowed subaqueous free-growth of coarse crystals at the brine-sediment interface (Bąbel, 2007; Ortí, 2011). In this depositional system, shallowness is supported by the well stratified bedding which probably records repetitive fluctuations of the water salinity (Bąbel, 2007). The crystals were preferentially growing in a vertical position and the competitive growth of the selenites induced crystallization stresses that resulted in the domal shape of some beds (Castens-Seidell, 1984; Hardie and Eugster, 1971). The rippled and non-oriented crystalline gypsum layers mixed with muddy material probably resulted from the reworking of selenites beds by storm events. Anhydritisation features, limited to tabular beds, may have formed during the most arid periods, when the pond was entirely desiccated or when the salinity of the pond was highly increased (Bąbel, 2007; Kasprzyk, 2003; Shearman, 1978). On the opposite, when the salinity of the pond was temporarily decreased, the gypsum crystallization was stopped and the calcite layers could precipitate.

e. Facies association 5: Massive secondary gypsum

Description: FA 5 corresponds to tabular and continuous gypsum beds, 10 centimeters to several meters-thick (Fig. 6), displaying an alabastrine texture (milky-like gypsum, Fig. 6 A) that may laterally and vertically evolve to a texture made up of enterolithic folds and amalgamated centimeter- to decimeter-thick nodules (Fig. 6 B). The gypsum beds can be stacked over up to several tens of meters (Fig. 6 D). In these thick intervals, a centimeter- to decimeter-thick layering may be marked by thin (< 0.5 cm) and continuous to discontinuous interlayers of green clays or grey carbonates, variably brecciated in the gypsum (Fig. 6 D and E). Such beds can scarcely display ghost of selenite crystals up to 3 cm-thick (Fig. 6 F). Thin section observations in the gypsum reveal radiated anhydrite laths being replaced by amoeboid gypsum or porphyroblastic to xenotopic gypsum with remaining relicts of very altered anhydrite crystals (Fig. 6 G and H).

Interpretation: Amalgamated nodules and anhydrite laths observed on the thin sections are commonly attributed to primary gypsum deposits having been intensively dehydrated into anhydrite, whereas replacive ameboid gypsum evidences later rehydration of anhydrite into gypsum (Hussain and Warren, 1989; Kasprzyk, 2003; Rouchy et al., 1986). The local preservation of selenite shapes and the poor clay-content suggest that part of the primary gypsiferous deposits belonged to FA 4 (e.g. Warren and Kendall, 1985a). Conversion from gypsum to anhydrite could have occurred at shallow to moderate burial depth during temperature increase (> ~ 50-60°C) (Murray, 1964; Shearman, 1978; Warren, 1991, 2010; Warren and Kendall, 1985b). Alternatively, sabkha processes during long-lasting desiccation event with fluctuation of the water table could have as well contributed to develop primary and/or replacive nodular anhydrite under high salinity condition (Gindre-Chanu et al., 2015). Later rehydration probably occurred during exhumation of the basin, when anhydrite was pervasively rewatered in the shallow zone of active phreatic flow (*e.g.* Gindre-Chanu et al., 2015).

f. *Facies association 6: Isolated to coalesced nodular gypsum*

Description: This FA is characterized by decimeters to 1 meter-thick intervals displaying millimeters to decimeters-thick isolated to coalesced gypsum nodules within laminated green clays composing ~60% of the FA (Fig. 7, A, B). The nodules are displacive, highly irregular in shapes and size, aligned in to the bedding or chaotically organized (Fig. 7, A, B).

Interpretation: The gypsum nodules are interpreted as having precipitated in the capillary fringe of a dry and muddy soil profile trough evaporitic pumping of the groundwater (e.g. Ali and West, 1983; Hussain and Warren, 1989; López-Quirós et al., 2018). This FA is thus interpreted as having formed in long lasting periods of desiccation, in a sabkha-like environment (Aref et al., 1997; Schreiber and El Tabakh, 2000; Warren and Kendall, 1985a).

g. *Facies association 7: Siliciclastic-rich gypsum*

Description: This facies association is characterized by decimeter to 1 meter-thick tabular to channelized beds made up of a massive to friable gypsum enclosing siliciclastic grains and pebbles and interlayered with reddish shales (Fig. 7 C, D and E). Channels are several meters wide and the pebbly facies are rich in isolated to coalesced gypsum nodules up to 3 cm-thick (Fig. 7 D). The beds locally display a normal grading as well as plane parallel laminations and tabular to cross-stratifications (Fig. 7 A).

Interpretation: This FA is interpreted as characterizing reworked evaporitic deposits, i.e. gypsrudite to gypsarenite. The massive to friable texture results from multiple episodes of dehydration and hydration processes during burial and exhumation (see FA 5, Hussain and Warren, 1989; Shearman, 1978). The primary texture of the clastic gypsum is thus not preserved in this facies, but inferred from (i) the occurrence of the detrital siliciclastic-grains and pebbles and (ii) from the gypsum nodules found in the pebbly beds, interpreted as reworked gypsum clasts which suffered as well from diagenetic transformations (Testa and Lugli, 2000). Such clastic evaporites were probably produced by flood events, which sourced the non-evaporitic content and reworked lacustrine to sabkha evaporites, or alternatively, by the mechanical reworking of the diapiric evaporites surrounding the minibasins (Lawton and Buck, 2006).

h. Post depositional solution related breccia

Description: This facies is characterized by several meter-thick strata intervals made up of faulted, brecciated and folded gypsum beds of the FAs 1 to 4 (Fig. 7 F to I). The brecciated intervals are laterally extended over all the available outcrop and deformation intensity decrease upward in each interval. The gypsum layers below the brecciated section are not affected by noticeable deformations.

Interpretation: The deformations of this facies are interpreted as characterizing collapse breccias resulting from the dissolution of former interlayers of highly soluble evaporites, most probably halite (e.g. Bąbel, 1991; Testa and Lugli, 2000). It is not possible to constrain in which environment (subaqueous or subaerial) this halite precipitated.

2. Synthesis of depositional environments

The dominant FAs 1 to 4 characterize a similar relatively shallow water setting in which the salinity saturation controlled the amount and the primary crystalline texture of gypsum (Fig. 8). FA 1 developed during stratigraphic intervals marked by a brackish lake with undersaturated conditions preventing evaporite precipitation. With increasing salinity conditions, together with decreasing clastic inputs, gypsiferous FAs 2, 3 and then 4 could then successively develop in the same dominantly subaqueous environment. Such successive steps of gyspsiferous facies evolutions due to salinity increase are especially observed in 5 of the 8 evaporitic units logged in the Inceyol minibasin, except that FA 4 was transformed into FA 5 due to early or late diagenetic transformations (Fig. 8).

Under extreme salinity conditions, halite deposits were also able to precipitate and their subsequent dissolution resulted in post-depositional collapse breccias. Long-lasting desiccation event might have temporary favored sabkha processes of FA 6, and flood events could sometime be strong enough to produce siliciclastic-rich gypsarenite and gypsrudite deposits such as FA 7 (Fig. 8).

The occurrence of each evaporitic facies was eventually dependent of the balance between the climate aridity and the restriction to fluvial inputs, this latter being halokinetically-controlled (Ribes et al., 2018, 2016; Banham and Mountney, 2013a). Moreover, it is not excluded that different FAs were laterally equivalent in the EMBs (e.g. selenitic gypsum crust of FA 4 located in basin center and laterally grading to sabkha deposits of FA 6 in basin border; e.g. Eugster and Hardie, 1978; Abrantes *et al.*, 2016). However, such variations could not be observed due to outcrop conditions and meteoric alteration of the evaporitic deposits.

C. Internal deformation structures

The EMBs display several internal deformational structures that evidence diapir-sediment interactions during the subsidence of the minibasins. These structures are summarized by focusing on representative EMBs examples. Specific features compared to other non-evaporitic minibasins of the Sivas Basin and in other halokinetic settings are also highlighted below.

1. Sedimentary wedges and halokinetic sequences: example of the Koyuncu minibasin

Description: With the exception of the Cekmis minibasin, all the EMBs display sedimentary wedges flanking their diapiric borders, among which the Koyuncu minibasin (Fig. 9 A) shows the most striking ones. This minibasin shows a tight, asymmetric and contorted synclinal shape (Fig. 9 B). Along its western, northern and eastern flanks, the strata are folded and thinned over a distance of 50 to 500 meters from the diapiric wall, with bed rotations reaching up to 140° (Fig. 9 B, C, D, E). It should be noted that the sedimentary wedges of the Koyuncu minibasin are not only localized at salt wall-sediment interface but all over the minibasin.

The sediment-diapir contacts are also locally characterized by the occurrence of halokinetic sequences (sensu Giles and Rowan, 2012). The best example of such structures can be observed along the north-eastern corner of the Koyuncu minibasin, where the satellite image highlights steepened strata displaying a hook-like fold unconformably capped by younger strata (Fig. 9 B). The hook shows a drape folding of less than 200 meters amplitude, is capped by a 90° angular unconformity and shows limited sedimentary thinning. The younger strata display a well-expressed folded sedimentary wedge in which we might as well spot discrete erosive surfaces (i.e. progressive unconformities) but with angular unconformities lower than 30° (Fig. 9 A and B).

Interpretation: The sedimentary wedges demonstrate the progressive bed rotation of the evaporitic deposits during their subsidence in the minibasin, and thus, the syn-sedimentary growth of the diapiric evaporites (e.g. Andrie et al., 2012; Poprawski et al., 2014). Moreover, the 3D asymmetric geometry of the minibasin and its bed orientations suggest the occurrence of an asymmetric synclinal depocentre with a basin-ward dipping growth strata at depth, as proposed on figure 9 F. Such a geometry suggests that bed rotation did not only occur because of relative diapir rise along minibasin borders, but have resulted from the westward tilting of the minibasin floor together with lateral flow of the evaporites below the minibasin. The development of a prograding sedimentary roll-over could have triggered the minibasin tilting, but such a process is commonly tied to large-scale prograding siliciclastic or carbonate systems (e.g. Ge et al., 1997; Kergaravat et al., 2017) and seems unlikely in the small-scale lacustrine evaporitic system of the EMBs . Accordingly, we rather interpret the asymmetric synclinal geometry of the Koyuncu minibasin as having been driven by other mechanisms of subsidence that might have involved the influence of (i) compressive strains having resulted in the preferential uplift of the eastern diapiric wall, (ii) a base-salt relief with or without translation of the minibasin during compression (Kergaravat et al., 2017; Kluth and Du Chene, 2009) and (iii) the asymmetric flow of diapiric salt influenced by the subsidence of surrounding siliciclastic minibasins (Fernandez et al., 2019; Hudec et al., 2009; Kergaravat et al., 2017; Kluth and Du Chene, 2009). Following 2D numerical models recently performed by Fernandez et al. (2019), this last hypothesis seems especially supported by the fact that the Koyuncu mini-basin tilted westward, i.e., away from the three other siliciclastic mini-basins surrounding the EMB, where the diapiric salt could more easily and rapidly flow (Fig. 2 A and 9).

The geometries, wedge thickness and architectural patterns of halokinetic sequences usually account for interplays between the salt-flow rate and the sedimentation rate of the recycled evaporites (Giles and Rowan, 2012; Rowan et al., 2003). The hook-fold at the base on the Koyuncu minibasin especially highlight a period during which the diapir flow rate temporarily exceeded the precipitation rate of evaporites, allowing the flowing evaporites to reach the surface (Giles and Rowan, 2012). The coeval westerly stacked sedimentary wedges with low-angle unconformities could form tapered composite halokinetic sequences (sensu Giles and Rowan, 2012). Such sequences would highlight that, despite relative fluctuation between the diapir-rise rate and evaporite precipitation, the overall precipitation rate of evaporites remained higher than the diapir-rise rate, preventing the diapir to ever reach the surface by uplifting enough its sedimentary roof (Giles and Rowan, 2012).

2. Folds and faults: example of the Köy and Cekmis minibasins

Description: Over the first 100 meters of the EMBs borders, tight folds and reverse faults are frequently observed, such as in in the Köy and Koyuncu minibasins (Fig. 10). Fold axes can be parallel to the adjacent diapiric wall, or more chaotically oriented. The sedimentary infill of the minibasins is also affected by small-scale normal faults displaying meter-scale offsets (Fig. 10 C).

In the Cekmis minibasin (Fig. 11 A and B), the large extent of folding and faulting stands out from other EMBs. The western side of the minibasin lies on a diapiric unit and its southern part is steeply delimited by a vertical fault. The presence of a sinuous vertical weld is inferred along the north-eastern border of the minibasin according to (i) the geometry of strata that are steep to overturned, (ii) the occurrence of an erosive surface above overturned evaporites, suggesting an halokinetic sequence, and (iii) a hook fold and associated sedimentary wedge in the alluvial conglomeratic deposits along the northern side of the weld (Fig. 11 B, C). The core of the inferred weld is marked by shales densely affected by gypsum-filled fractures with sheared gypsum blocks. On its western part, basal evaporitic deposits of the minibasin are 90° tilted (Fig. 11 A and B). There, satellite images clearly highlight two, 400 meters-long, faults (NW-SE oriented), which merge at the contact with the diapiric core bounding the minibasin base, and which define two tilted blocks, with an offset of approximately 100 meters. Eastward, these normal faults are sealed by vertical and intensely folded evaporitic strata (Fig. 11 A and B). At a regional scale, within the folded area, fold axes tend to be parallel to the western and north-eastern borders of the minibasin, and the main synclines and anticlines mapped on figure 11 B are not representative of the folding complexity observed at the outcrop scale (Fig. 12 A). Finally, along the eastern border of the minibasin, within the youngest deposits, we also note a thick accumulation of reworked evaporitic facies with channelized gypsarenites and conglomerates of the FA 7 (Fig. 7 C and D).

Interpretation: As previously described, the folds and faults may result from collapse structure controlled by the dissolution of former halite interlayers. However, the preferential occurrence of such deformations along the minibasin borders and the absence of brecciated evaporites rather suggest a different origin. Indeed, the folds can be interpreted as (i) gravitational slumps related to the steepening of the evaporitic strata (especially when fold axes are oriented parrallel to the bordering diapiric wall, e.g. Alsop *et al.*, 2000; Trude *et al.*, 2012) and/or as (ii) deformations related to the squeezing of the diapiric wall as a result of tectonic shortening in the Sivas Basin. On the other hand, the normal faults probably accommodated the fast subsidence of the EMBs together with the uplift of the minibasin borders (Alsop et al., 2000; Kergaravat, 2016), as they generally shows unidirectional dip direction away from the inferred diapir or wall topographic high.

Accordingly, the faults of the Cekmis minibasin are interpreted to have formed originally as normal faults (before being verticalized up to their outcropping position), and the folds as aerial slumps (Fig. 12 B). These gravitational structures would be related to the eastward tilting of the overall minibasin. According to this scenario, the growth of a diapiric relief along the western border of the minibasin triggered the normal faulting (due to outer-arc extension) until the slope became steep enough to induce the eastward collapsing of the evaporitic strata as mega slumps. The normal faults are thus sealed by the basal decollement surface of the slumped deposits (Fig. 12 B). The following erosion of the steepened and folded deposits probably sourced the gypsrudites to gypsarenites observed along the eastern border of the Cekmis minibasin.

3. Overturned flap: the example of the Devrik minibasin

Description: The Devrik minibasin displays evaporitic deposits with tilted flanking strata drawing a simple synclinal shape, as commonly observed in the other EMBs (Fig. 13 A). However, along the northeastern border of the minibasin, from the north to the east, the evaporitic strata progressively steepen and become overturned up to a 180° rotation over 600 meters (Fig. 13 B and C).

Interpretation: Although the lacustrine to sabkha facies of the evaporites makes the determination of bed polarity difficult, all the northeastern border of the minibasin appears overturned as compared to the rest of the minibasin. Accordingly, the Devrik minibasin displays the structure of an inverted flap (Fig. 13 D) (Callot et al., 2016; Graham et al., 2012; Rowan et al., 2016). The evaporitic deposits were likely overlying the diapiric stem along its eastern border, before being tilted and inverted by diapiric inflation and salt sheet emplacement. The latter was probably quite poor in insoluble residues (increasing its ability to extrude rapidly) and its dissolution plus erosion did not leave any residual material on outcrop.

4. Internal diapiric deformations

a. Central diapiric stem: example of the Inceyol minibasin

Description: The Inceyol minibasin displays a tight, closed synclinal shape with tilted to overturned strata along its western, northern and eastern borders, forming a teardrop geometry (Fig. 14). The centre of the minibasin has the peculiarity of being penetrated by a small diapiric stem linked to the western diapiric wall of the minibasin. The central diapir progressively pinches out toward the north, and closes at the junction between two tight peripheral synclines arranged around the diapiric stem (Fig. 14).

Interpretation: The central diapiric structure is interpreted as a former local topographic high on the surface of the diapir that existed in the early stage of the minibasin development. Alternatively, this local structure might have separated two initial depocenters that finally coalesced during the evolution of the EMB. During the subsidence and late exhumation of the EMB, compressive tectonic strains most possibly contributed to (i) develop the topographic relief into a small-scale diapiric stem that finally got squeezed (Kergaravat et al., 2017), and (ii) tighten the minibasin up to its final highly encased geometry.

b. The proto minibasins of the Fadlun diapir

Description: To the east of the Devrik minibasin, the Fadlun diapir is covered by patches of lacustrine to sabkha deposits forming 6 rafts distributed chaotically and disconnected by few hundred meters of diapiric evaporites (Fig. 15). The rafts are 100 to 300 meters-large and up to 1.3 kilometers-long, with a sediment thickness that can hardly be constrained but which can be estimated to be of few hundred meters for the bigger one in the central part (Fig. 15). These deposits are folded, display highly irregular contours and do not show mature minibasins structures such as those described above (Fig. 15).

Interpretation: Two hypotheses can explain the origin of such distributed evaporitic accumulations. They may have constituted a former evaporitic sedimentary cover that has been fragmented, brecciated and deformed by diapir inflation (e.g. Dooley et al., 2015a). Otherwise, the lacustrine to sabkha sediments were initially deposited in isolated small-scale depocenters, partly disconnected by topographic reliefs on the roof of the diapir, such as it was proposed for the early stage of the Inceyol minibasin. In both cases, such deposits would represent the relics of one to several EMBs that have been aborted early due to the rejuvenation of the diapir. Such a stronger upward flow of the salt compared to minibasin subsidence might have been caused by (i) tectonic shortening and associated squeezing of the diapir (Duffy et al., 2018; Kergaravat et al., 2017), (ii) subsidence of the surrounding minibasins, especially the coeval evaporite-rich Devrik minibasin westward (Fernandez et al., 2019). Lateral expansion of the diapir topography in response to spreading under its own weight then also probably contributed to fragment and folding the evaporitic raft (Dooley et al., 2015a; Duffy et al., 2018).

V. Discussion

1. Initiation of the evaporite-rich minibasin

In order for the EMBs to start developing in the Sivas Basin, the following factors must have been met: (i) a semi-arid climate together with limited fluvial or marine inputs allowing evaporite precipitation conditions to prevail (evaporation > water input), (ii) a source of dissolved salt allowing thick evaporitic accumulations in response to the former factor, and (iii) an outcropping diapiric body with an almost flat top allowing to be capped by evaporites (Fig. 16 A).

In the Sivas Basin, the climatic and hydrologic conditions were favorable to evaporite precipitation during the Oligo-Miocene (Çiner et al., 2002; Ribes, 2015) and the salt-induced topographic reliefs likely increased the hydrographic isolation of some EMBs (Ribes et al., 2018, 2016). Also, as evidenced by Pichat et al. (2018), the dissolved elements necessary for significant accumulations of evaporites were provided in abundance by the leaching of the diapiric structures themselves. The dissolution of the diapiric bodies could occur at the surface, along the outcropping diapiric walls bordering the EMBs. Alternatively, it could have occurred in the sub-surface (e.g. Rodriguez et al., 2017), producing saline springs at surface, such as those presently observed in several locations of the Sivas Basin (Fig. 8) (Gunay, 2002; Kaçaroğlu et al., 2001; Pichat et al., 2018).

Several factors may then have simultaneously allowed the diapiric bodies to be covered by evaporitic facies. First, Ribes et al. (2016) have shown that the Unit 2 and 3 of the Karayün Formation recorded a period of high regional accommodation and sedimentation supply, superimposed on salt-controlled accommodation, prone to the burial of diapirs under continental sediments. More recently, Kergaravat et al. (2017) have also proposed that some of the EMBs they identified west of the Emirhan minibasin were located within relay systems of a transtensive zone, where the diapirs could be locally deflated in pull-apart systems. Without extension, the diapir stems might simply have stopped rising due to the decrease in the evaporite sourcing at depth, as the mother salt was locally welded below the surrounding primary minibasins. It is also probable that the surface and subsurface dissolution of the diapiric salt significantly contributed to the deflation of the diapirs. Moreover, the capping of the diapirs could have been promoted by previous erosion and flattening during the deposition of the coarse fluvial sediments which preceded the two episodes of evaporite deposition (i.e. Unit 2 of the Karayün Formation and Unit 1 of the Benlikaya Formation, Ribes et al., 2016, 2018). Finally, the covering of the diapirs have certainly been also favored by the high sedimentation rates characteristic of evaporitic environments (Rouchy and Blanc-Valleron, 2006; Warren, 2016), sustained in particular by the high supply in dissolved elements provided by the nearby diapirs (Fig. 16 A) (Pichat et al., 2018).

2. Evaporite-rich minibasin infill and subsidence

Once the diapirs were covered by recycled evaporites, local extensive stress (Kergaravat et al., 2017) and / or sustained surface and subsurface dissolution of the diapiric salt (Pichat et al., 2018) could have maintained subsidence of the EMB together with their filling by recycled evaporites (Fig. 16 B). Depending on the climate and the hydrology, and by analogy with modern outcropping diapirs in arid to semi-arid climate (in Iran and Israel especially), dissolution and induced subsidence rate of the diapiric salt might have been on the order of 0.5 millimeters to few centimeters per year (Bruthans et al., 2010, 2009; Frumkin, 2000, 1994; Galve et al., 2009; Roosta et al., 2019; Zarei et al., 2012).

Different timing of evaporite dissolution vs deposition might have occurred. The dissolution of exposed diapiric evaporite occurred during humid periods or seasons, before deposition of recycled evaporites during dryer periods. On the opposite, subsurface dissolution of diapiric salt could have been permanently coeval with the deposition of the new evaporites in the minibasins. If climatically-controlled (e.g. Ocakoğlu et al., 2017), coeval EMBs might share the exact same sedimentary stratal pattern and facies evolution. Alternatively, if controlled by halokinetically-influenced fluvial inputs (e.g. Banham and Mountney, 2013b; Ribes et al., 2016), each minibasin might have recorded its own salinity fluctuation and related evaporite depositional cycles. Detailed stratigraphic correlations would be necessary do decipher such an issue, which could unfortunately not be performed in the frame of this study.

The high density of the sulphate-rich evaporites also probably played a key role in driving a fast subsidence of the minibasin. Indeed, the densities of gypsum (2.2 - 2.4 g/cm^3) and of anhydrite (2.9 - 3.0 g/cm^3) are higher than that of halite (2.1 - 2.2 g/cm^3) and of poorly buried siliciclastic sediments (< 2.2 g/cm^3 above ~800 - 1000 m depth; e.g. Jackson and Talbot, 1986; van den Belt and de Boer, 2007; Hudec *et al.*, 2009). Accordingly, Fernandez et al. (2017) recently demonstrated that only a small amount of gypsiferous deposits could considerably enhance the subsidence of minibasins by dramatically reducing the depth of density inversion between the salt diapir and the minibasin overburden. The high proportion of gypsum-anhydrite beds in the EMBs strongly suggests the efficiency of density driven subsidence (Fig. 16 B).

Finally, because gypsum deposits can precipitate at an average rate of 1 cm/year (Warren, 2016), it is noteworthy that the recycled gypsiferous deposits in the EMBs could have easily compensated (in addition to inducing) subsidence rates which can be also as high as 1 cm/year (Prather, 2000).

3. Influence of evaporite rheology

We have highlighted that the EMBs are structurally characterized by (i) their small dimension with an encased morphology and (ii) the variety of their internal deformations that include halokinetic sequences, well-developed sedimentary wedges, gravitational slumps and overturned flap.

Small-scale encased minibasins with the same dimension to those of the Sivas EMBs (0.5 to 2 km wide) are actually uncommon in the literature, and the rare analogies that we were able to find involve mud-rich deposits in distal margin settings (Fort et al., 2004) or other possible primary evaporite-rich mini-basins in the Precaspian (Fernandez et al., 2017).

Even if they are well developed in the EMBs, the halokinetic sequences and sedimentary wedges observed in the EMBs do not display characteristic evaporite-related pattern, compared to similar structures in the Sivas Basin (Kergaravat et al., 2017; Ribes et al., 2016, 2015) and in other halokinetic provinces (Hudec et al., 2009; Poprawski et al., 2016; Rowan et al., 2003; Volozh et al., 2003).

Slumped deposits such as those of the Cekmis minibasin have not been identified in surrounding siliciclastic minibasins of the Sivas Basin. Elsewhere, gravitational collapse structures above diapirs occur in marine settings where the water content of the sediments trigger their instability (Davison *et al.*, 2000; Pilcher and Blumstein, 2007; Madof *et al.*, 2009). However, compared to those of the EMBs, such slump intervals are commonly of higher-scale extension (over several kilometers) and produced debris-slide and debris flow deposits which were not observed in the EMBs of the Sivas basin.

The overturned flap observed in the Devrik minibasin does not have equivalence in other minibasins filled by siliciclastic deposits in the Sivas Basin (Kergaravat et al., 2017; Ribes et al., 2016). However, similar order of fold amplitude were reported in other halokinetic domains involving as well evaporitic deposits: (i) in evaporite-rich minibasins of the Precaspian Basin (Fernandez et al., 2017), (ii) in intrasalt shale-rich formations constituting the limb of the Sedom diapiric wall in the Dead Sea (Alsop et al., 2015) and (iii) in intrasalt diapiric deformation of thick evaporite accumulation in the Santos Basin, Brazil (Jackson et al., 2015).

All of such structural peculiarities of the Sivas EMBs, and the rare analogies with other mud- and evaporite-rich minibasins elsewhere, strongly suggest that the weak rheology of the evaporitic overburden significantly influenced the evolution of the minibasins. The low stiffness of the evaporite- and clay-rich overburden could probably not significantly prevent the rising of the bordering diapiric walls (i.e., no capacity of stopping the diapir rise by burring it), allowing their sustained growth over the time (e.g., Fernandez *et al.*, 2016). The borders of the minibasins were thus easily tilted and inverted, triggering the formation of slumps, flaps and sedimentary wedges, and facilitating the encasement of the minibasin in the deflating diapir (Fig. 16 C). The rapid subsidence and tilting of the minibasins, as previously discussed, probably also favored the minibasin encasement and deformation. Multiple detachment surfaces present in the layered evaporites might have as well facilitated slumping events.

VI. Conclusion

1) Evaporite-rich minibasin refer to mini-basins for which 50 to 100% of the sedimentary infill is composed of evaporite-rich facies. Despite their importance in halokinetic setting, such type of minibasins remains poorly understood. Some of them outcrop in the central halokinetic province of the Sivas Basin and were studied on the field.
2) The evaporite-rich minibasins of Sivas developed above deflating diapirs, during periods of limited fluvial input when the diapiric structures were outcropping with insignificant topography. The minibasins were filled by more than 50 % of lacustrine gypsiferous facies recycled from the dissolution / re-precipitation of the diapiric salt.
3) The capping of the diapiric stems by recycled evaporites was promoted by (i) periods of high regional accommodation, (ii) erosion of the diapiric crests by the fluvial system preceding evaporite deposition, (iii) deflation of the diapirs following local transtensive stress and / or by surface to subsurface salt dissolution, and (iv) fast sedimentation rate of the evaporites. Subsequent development of the evaporitic minibasin was then probably primarily driven by the high density of gypsum and anhydrite in the overburden, compared to halite in the diapirs.
4) Compared to other siliciclastic minibasins of the Sivas Basin, the evaporite-rich minibasins stand out by (i) their small dimension (< 1 km), (ii) their teardrop encased shape and (iii) amplified internal halokinetic deformations. The latter especially include well-developed halokinetic wedges, mega-slumps or inverted flaps. It is suggested that such structural specificities were favored by the ductile rheology of the evaporitic overburden.
5) Although secondary evaporite-rich minibasins have never been identified in other ancient halokinetic settings, our study emphasizes that they may have developed under arid continental or coastal environments. Such secondary evaporitic minibasins, and the primary ones already inferred in other halokinetic provinces, could share the structural and sedimentologic peculiarities highlighted in the evaporite-rich minibasins of the Sivas Basin.

Acknowledgment:

The authors thank Total SA for their financial support in the frame of the Structural Geology chair (JP Callot) at E2S UPPA. We are also grateful to S. K. Kavak, C. Kergaravat, C. Ribes, E. Legeay, M. Larrey, V. Navelot and G. Calinak for their assistance during the field work. We thank J.M. Rouchy for having introduced us in the study of evaporitic deposits. We finally thank L. Gindre-Chanu, M. Pichel, S. Banham and one anonymous reviewer whose remarks and corrections greatly contributed to improve the manuscript.

Figures caption

Figure 1: Tectonic map of Eastern Mediterranean, with the main continental blocks (differentiated by grey tints), major suture zones and the Oligo-Miocene Sivas basin deposits (after Ribes et al., 2015a modified from Okay et al., 2006). BZSZ: Bitlis-Zagros Suture Zone, EAF**:** East Anatolian Fault Zone, IAES: Izmir-Ankara-Erzincan Suture Zone, ITSZ: Inner-Tauride Suture Zone, NAF**:** North Anatolian Fault.

Figure 2: A: Geological map of the study area with the location of the identified evaporitic minibasins (after Kergaravat et al., 2017; Legeay et al., 2019b). B: Regional composite lithostratigraphic column of the central Sivas Basin, with average thickness of the various stratigraphic units (after Legeay et al., 2019b). C: Cross-section of the central halokinetic domain of the Sivas Basin (after Kergaravat et al., 2017)

Figure 3: Sedimentary log of the Inceyöl minibasin with illustration of the facies associations in the gypsiferous units.

Figure 4: **A:** Clay-rich stratigraphic interval displaying green to red clays interlayered with carbonate beds (white dots) and a sand body (yellow dots). **B:** Laminated green to grey carbonaceous shales interlayered with a thin sandstone bed (yellow dots). **C:** Carbonate bed with molds of former gastropod fossils (yellow arrows). **D:** Thin section of a carbonate bed showing numerous charophyte and shell fragments. The pink arrows point gyrogonite fragments of charophytes. The yellow arrow points a preserved ostracode shell (optical photomicrograph, PPL). **E:** Wave ripples in a fine sandstone bed. **F and G:** Examples of laminated banded gypsum and clay layers of FA2. The black arrow on picture F points a highly crenulated gypsum layer. The pink arrows points discontinuous gypsum layers displaying bowl-shapes. The yellow arrow on picture F points to clay layers displaying tiny gypsum nodules. The yellow arrows on picture G point to teepee-like shapes. **H and I:** Examples of nodular banded gypsum layers of FA3. The yellow dots on picture H highlight discrete erosive surfaces cutting the crest of mushroom-like shapes made up of entherolithic gypsum (black dots). The yellow arrow on picture I points a gypsum layer displaying a highly crenulated top. The pink arrow points a gypsum layer with vertically-aligned tiny nodules.

Figure 5: **A:** Selenitic gypsum accumulations interbedded with thin carbonates layers (yellow arrows). Note (i) the displacive nodular gypsum beds in the bottom part of the picture (pink arrows), (ii) the whitened crystalline bed in the middle part (black arrow) and the dome-like shapes of some beds (green arrow). **B:** Selenitic gypsum crust with upward oriented crystals and dome-like shapes. **C and D:** Non-oriented selenitic gypsum crystals embeded in a micritic matrix. **E:** Wavy ripple marks in tiny non-oriented gypsum crystals.

Figure 6: **A:** Massive alabastrine gypsum. **B:** Nodular and entherolithic gypsum to anhydrite. **C:** Continuous tabular gypsum beds of alabastrine texture interlayered with clays. **D:** Thick accumulations of alabastrine to nodular gypsum beds. Note the distinguishable layering. **E:** Layered alabastrine gypsum displaying a thin and brecciated carbonate bed (yellow arrow). **F:** Ghost of selenitic gypsum crystals in an alabastrine gypsum layer. **G:** Anhydrite laths (left, An) partly replaced by amoeboid gypsum (right, G) (optical photomicrograph, XPL). **H:** Xenotopic gypsum (G) enclosing relics of anhydrite crystals (optical photomicrograph, XPL).

Figure 7: **A and B:** Isolated to coalesced gypsum nodules within laminated green clays. Picture A illustrates a stratigraphic surface. **C to E:** Siliciclastic-rich and channelized coarse-grained gypsum beds. Note the parallel and cross-stratifications on picture C. The nodules on pictures D are interpreted as former gypsum pebbles. **F to I:** Stratigraphic interval displaying folded, brecciated and sheared massive to banded-laminated gypsum beds.

Figure 8: Synthesis of the depositional evaporites in an evaporite-rich minibasin of the Sivas Basin.

Figure 9: **A** and **B:** Google Earth satellite image and geological map of the Koyuncu minibasin (see figure 1 C for location of the minibasin). The white square on picture B highlights a hook-fold probably forming a halokinetic sequence. **C, D**, and **E:** Panoramas of the sedimentary wedges and of the synclinal shape of the Koyuncu minibasin (see A for location of the panoramas). **F:** Cross section of the Koyuncu minibasin (see figure 11 B for location of the cross-section).

Figure 10: Satellite images (A and D) and field pictures (B and C) of the small-scale folds and faults observed along the diapiric borders of the Koy minibasin (A to C) and the Koyuncu minibasin (D, see figure 1 C and 11 B for the location of the satellite image).

Figure 11: **A** and **B:** Google Earth satellite image and geological map of the Cekmis minibasin (see figure 1 C for location of the minibasin). **C**: Panorama of the weld inferred along the eastern border of the Cekmis minibasin. The black arrows point to the top of the beds. The dotted black line represents an erosive surface marking the transition from the Benlikaya Formation to the Injesu Formation.

Figure 12: **A:** Tight folds within the evaporitic facies (see figure 13 A for location of the picture). **B:** Cross-section the Cekmis minibasin (see figure 13 B for location of the cross-section).

Figure 13: **A** and **B:** Google Earth satellite image and geological map of the Devrik mini-bassin (see figure 1 C for location of the minibasin). **C:** Panorama of the Devrik mini-bassin (see A for location of the panorama). **D**: Cross-section of the Devrik minibasin (see B for location of the cross-section).

Figure 14: **A** et **B:** Google Earth satellite image and geological map of the Inceyol minibasin (see figure 1 C for location of the minibasin). **C:** Panorama of the Inceyol minibasin (see A for location of the panorama). **D**: Cross-section of the Inceyol minibasin (see picture B for location of the cross-section) (Modified after Kergaravat et al., 2017).

Figure 15: Interpreted Google Earth satellite image of the Fadlun diapir (see figure 2A for location of the picture).

Figure 16: Synthesis of the main factors that might have triggered the initiation, subsidence and deformation of evaporite-rich minibasins in the Sivas Basin.

References

Abrantes, F.R., Nogueira, A.C.R., Soares, J.L., 2016. Permian paleogeography of west-central Pangea: Reconstruction using sabkha-type gypsum-bearing deposits of Parnaíba Basin, Northern Brazil. Sediment. Geol. 341, 175–188. https://doi.org/10.1016/j.sedgeo.2016.06.004

Aktimur, H.T., Tekirli, M.E., Yurdakul, M.E., 1990. Geology of the Sivas-Erzincan Tertiary basin. Miner. Resour. Explor. Bull. 111, 21–30.

Al-siyabi, H.A., 2005. Exploration history of the Ara intrasalt carbonate stringers in the South Oman Salt Basin. GeoActa 10, 39–54.

Ali, Y.A., West, I., 1983. Relationships of modern gypsum nodules in sabkhas of loess to compositions of brines and sediments in northern Egypt. J. Sediment. Res. 53, 1151–1168. https://doi.org/10.1306/212F8332-2B24-11D7-8648000102C1865D

Alsop, G.I., Brown, J.P., Davison, I., Gibling, M.R., 2000. The geometry of drag zones adjacent to salt diapirs. J. Geol. Soc. London. 157, 1019–1029. https://doi.org/10.1144/jgs.157.5.1019

Alsop, G.I., Weinberger, R., Levi, T., Marco, S., 2015. Deformation within an exposed salt wall: Recumbent folding and extrusion of evaporites in the Dead Sea Basin. J. Struct. Geol. 70, 95–118. https://doi.org/10.1016/j.jsg.2014.11.006

Altunsoy, M., Özçelik, O., 1998. Organic facies characteristics of the Sivas Tertiary Basin (Turkey). J. Pet. Sci. Eng. 20, 73–85. https://doi.org/10.1016/S0920-4105(97)00051-X

Andrie, J.R., Giles, K.A., Lawton, T.F., Rowan, M.G., 2012. Halokinetic-sequence stratigraphy, fluvial sedimentology and structural geometry of the Eocene Carroza Formation along La Popa salt weld, La Popa Basin, Mexico. Geol. Soc. London, Spec. Publ. 363, 59–79.

Arakel, A. V., 1980. Genesis and Diagenesis of Holocene Evaporitic Sediments in Hutt and Leeman Lagoons, Western Australia. J. Sediment. Res. 50, 1305–1326. https://doi.org/10.1306/212F7BDF-2B24-11D7-8648000102C1865D

Aref, M.A.M., Attia, O.E.A., Wali, A.M.A., 1997. Facies and depositional environment of the Holocene evaporites in the Ras Shukeir area, Gulf of Suez, Egypt. Sediment. Geol. 110, 123–145. https://doi.org/10.1016/S0037-0738(96)00080-2

Artan, Ü., Sestini, G., 1971. Geology of the beypinari-karababa area (Sivas Province). Bull. Miner. Res. Explor. (Ankara, Turkey) 76, 72–89.

Bąbel, M., 2007. Depositional environments of a salina-type evaporite basin recorded in the Badenian gypsum facies in the northern Carpathian Foredeep. Geol. Soc. London, Spec. Publ. 285, 107–142. https://doi.org/10.1144/SP285.7

Bąbel, M., 1991. Dissolution of halite within the Middle Miocene (Badenian) laminated gypsum of southern Poland. Acta Geol. Pol. 41, 165–182.

Banham, S.G., Mountney, N.P., 2013a. Evolution of fluvial systems in salt-walled mini-basins: A review and new insights. Sediment. Geol. 296, 142–166. https://doi.org/10.1016/j.sedgeo.2013.08.010

Banham, S.G., Mountney, N.P., 2013b. Climatic versus halokinetic control on sedimentation in a dryland fluvial succession. Sedimentology 61, 570–608. https://doi.org/10.1111/sed.12064

Barde, J.-P., Chamberlain, P., Galavazi, M., Gralla, P., Harwijanto, J., Marsky, J., van den Belt, F., 2002. Sedimentation during halokinesis: Permo-Triassic reservoirs of the Saigak Field, Precaspian Basin, Kazakhstan. Pet. Geosci. 8, 177–187. https://doi.org/10.1144/petgeo.8.2.177

Belenitskaya, G., 2018. Salt Systems of the Earth: Distribution, Tectonic and Kinematic History, Salt-Naphthids Interrelations, Discharge Foci, Recycling. John Wiley & Sons.

Bobst, A.L., Lowenstein, T.K., Jordan, T.E., Godfrey, L. V., Ku, T.L., Luo, S., 2001. A 106 ka paleoclimate record from drill core of the Salar de Atacama, northern Chile. Palaeogeogr. Palaeoclimatol. Palaeoecol. 173, 21–42. https://doi.org/10.1016/S0031-0182(01)00308-X

Bruthans, J., Filippi, M., Asadi, N., Zare, M., Šlechta, S., Churáčková, Z., 2009. Surficial deposits on salt diapirs (Zagros Mountains and Persian Gulf Platform, Iran): Characterization, evolution, erosion and the influence on landscape morphology. Geomorphology 107, 195–209. https://doi.org/10.1016/j.geomorph.2008.12.006

Bruthans, J., Filippi, M., Zare, M., Churáčková, Z., Asadi, N., Fuchs, M., Adamovič, J., 2010. Evolution of salt diapir and karst morphology during the last glacial cycle: Effects of sea-level oscillation, diapir and regional uplift, and erosion (Persian Gulf, Iran). Geomorphology 121, 291–304. https://doi.org/10.1016/j.geomorph.2010.04.026

Callot, J., Ribes, C., Kergaravat, C., Bonnel, C., Temiz, H., Poisson, A., Vrielynck, B., Salel, J.F., Ringenbach, J.C., 2014. Salt tectonics in the Sivas basin (Turkey): crossing salt walls and minibasins. Bull. la Soc. Geol. Fr. 185, 33–42. https://doi.org/10.2113/gssgfbull.185.1.33

Callot, J., Salel, J., Letouzey, J., Daniel, J., Mengus, J., Pillot, D., Ringenbach, J., 2016. Three-dimensional evolution of salt-controlled minibasins: Interactions, folding, and megaflap development. Am. Assoc. Pet. Geol. Bull. 100, 1419–1442.

Castens-Seidell, B., 1984. The anatomy of a modern marine siliciclastic sabkha in a rift valley setting: Northwest Gulf of California tidal flats, Baja California, Mexico. PhD Thesis. Johns Hopkins University.

Cater, J.M.L., Hanna, S.S., Ries, A.C., Turner, P., 1991. Tertiary evolution of the Sivas Basin, central Turkey. Tectonophysics 195, 29–46. https://doi.org/10.1016/0040-1951(91)90142-F

Çiner, A., Kosun, E., Deynoux, M., 2002. Fluvial, evaporitic and shallow-marine facies architecture, depositional evolution and cyclicity in the Sivas Basin (Lower to Middle Miocene), Central Turkey. J. Asian Earth Sci. 21, 147–165. https://doi.org/10.1016/S1367-9120(02)00042-1

Clark, J.A., Stewart, S.A., Cartwright, J.A., 1998. Evolution of the NW margin of the North Permian Basin, UK North Sea. J. Geol. Soc. London. 155, 663–676. https://doi.org/10.1144/gsjgs.155.4.0663

Collon, P., Pichat, A., Kergaravat, C., Botella, A., Caumon, G., Ringenbach, J., Callot, J., Caumon, G., Ringenbach, J., Callot, J., 2016. 3D modelling from outcrop data in a salt tectonic context: Example from the Inceyol mini-basin, Sivas Basin, Turkey. Interpretation 4, 1–15. https://doi.org/10.1190/INT-2015-0178.1

Çubuk, Y., Inan, S., 1998. Imranli ve Hafik güneyinde (Sivas) Miyosen havzasinin stratigrafik ve tektonik Özellikleri. MTA Derg. 120, 45–60.

Davison, I., Alsop, G.I., Evans, N.G., Safaricz, M., 2000. Overburden deformation patterns and mechanisms of salt diapir penetration in the Central Graben, North Sea. Mar. Pet. Geol. 17, 601–618. https://doi.org/10.1016/S0264-8172(00)00011-8

Davison, I., Alsop, I., Blundell, D., 1996. Salt tectonics: some aspects of deformation mechanics. Geol. Soc. London, Spec. Publ. 100, 257. https://doi.org/10.1144/gsl.sp.1996.100.01.01

Davison, I., Anderson, L., Nuttall, P., 2012. Salt deposition, loading and gravity drainage in the Campos and Santos salt basins. Geol. Soc. London, Spec. Publ. 363, 159–174. https://doi.org/10.1144/SP363.8

Dilek, Y., Sandvol, E., 2009. Seismic structure, crustal architecture and tectonic evolution of the Anatolian-African Plate Boundary and the Cenozoic Orogenic Belts in the Eastern Mediterranean Region. Geol. Soc. London, Spec. Publ. 327, 127–160. https://doi.org/10.1144/SP327.8

Dooley, T.P., Jackson, M.P.A., Hudec, M.R., 2015a. Breakout of squeezed stocks: Dispersal of roof fragments, source of extrusive salt and interaction with regional thrust faults. Basin Res. 27, 3–25. https://doi.org/10.1111/bre.12056

Dooley, T.P., Jackson, M.P.A., Jackson, C.A., Hudec, M.R., Rodriguez, C.R., 2015b. Enigmatic structures within salt walls of the Santos Basin d Part 2 : Mechanical explanation from physical modelling. J. Struct. Geol. 75, 163–187. https://doi.org/10.1016/j.jsg.2015.01.009

Duffy, O.B., Dooley, T.P., Hudec, M.R., Jackson, M.P.A., Fernandez, N., Jackson, C.A.L., Soto, J.I., 2018. Structural evolution of salt-influenced fold-and-thrust belts: A synthesis and new insights from basins containing isolated salt diapirs. J. Struct. Geol. 114, 206–221. https://doi.org/10.1016/j.jsg.2018.06.024

Eugster, H.P., Hardie, L.A., 1978. Saline lakes, in: Leman, A. (Ed.), Lakes: Chemistry, Geology, Physics. Springer Berlin Heidelberg, pp. 238–388.

Fernandez, N., Dooley, T., Hudec, M.R., Peel, F., 2016. Evaluation of a halokinetic model for minibasin propagation, in: Applied Geodynamics Laboratory Conference 34.5.1. Austin, Texas.

Fernandez, N., Duffy, O.B., Hudec, M.R., Jackson, M.P.A., Burg, G., Jackson, C.A.L., Dooley, T.P., 2017. The origin of salt-encased sediment packages: Observations from the SE Precaspian Basin (Kazakhstan). J. Struct. Geol. 97, 237–256. https://doi.org/10.1016/j.jsg.2017.01.008

Fernandez, N., Hudec, M.R., Jackson, C.A.-L., Dooley, T.P., Duffy, O.B., 2019. The competition for salt and kinematic interactions between minibasins during density-driven subsidence: observations from numerical models. Pet. Geosci. In press. https://doi.org/10.31223/osf.io/jak5u

Fort, X., Brun, J., Chauvel, F., Ge, X.F., 2004. Salt tectonics on the Angolan margin, synsedimentary deformation processes. Am. Assoc. Pet. Geol. Bull. 8, 1523–1544. https://doi.org/10.1306/06010403012

Frumkin, A., 2000. Speleogenesis in salt – the mount Sedom area, Israel, in: Klimchouk, A. V., Ford, D.C., Palmer, A.N., Dreybrodt, W. (Eds.), Speleogenesis; Evolution of Karst Aquifers. Speleological Society of America, Huntsville, pp. 443–451.

Frumkin, A., 1994. Hydrology and denudation rates of halite karst. J. Hydrol. 162, 171–189. https://doi.org/10.1016/0022-1694(94)90010-8

Galve, J.P., Gutiérrez, F., Lucha, P., Bonachea, J., Remondo, J., Cendrero, a., Gutiérrez, M., Gimeno, M.J., Pardo, G., Sánchez, J. a., 2009. Sinkholes in the salt-bearing evaporite karst of the Ebro River valley upstream of Zaragoza city (NE Spain). Geomorphological mapping and analysis as a basis for risk management. Geomorphology 108, 145–158. https://doi.org/10.1016/j.geomorph.2008.12.018

Gamboa, L.A.P., Machado, M.A.P., da Silveira, D.P., de Freitas, J.T.R., da Silva, S.R.P., 2008. Evaporitos estratificados no Atlântico Sul: interpretaçao sísmica e controle tectono-estratigrafico na Bacia de Santos, in: Mohriak, W., Szatmari, P., Anjos, S.M.. (Eds.), Sal : Geologia e Tectônica -- Exemplos Nas Bacias Brasileiras. Beca Ediçoes Ltda, Sao Paulo, Brazil, pp. 340–359.

Ge, H., Jackson, M.P.A., Vendeville, B.C., 1997. Kinematics and dynamics of salt tectonics driven by progradation. Am. Assoc. Pet. Geol. Bull. 81, 398–423. https://doi.org/10.1306/522B4361-1727-11D7-8645000102C1865D

Giles, K.A., Rowan, M.G., 2012. Concepts in halokinetic-sequence deformation and stratigraphy, in: Alsop, G.I., Archer, S.G., Hartley, A.J., Grant, N.T., Hodgkinson, R. (Eds.), Salt Tectonics, Sediments and Prospectivity. Geological Society, London, Special Publication, pp. 7–31. https://doi.org/doi: 10.1144/SP363.2

Gindre-Chanu, L., Warren, J.K., Puigdefabregas, C., Sharp, I.R., Peacock, D.C.P., Swart, R., Poulsen, R., Ferreira, H., Henrique, L., 2015. Diagenetic evolution of Aptian evaporites in the Namibe Basin (south-west Angola). Sedimentology 62, 204–233. https://doi.org/10.1111/sed.12146

Görür, N., Tüysüz, O., Celal Şengör, a. M., 1998. Tectonic evolution of the Central Anatolian Basins. Int. Geol. Rev. 40, 831–850. https://doi.org/10.1080/00206819809465241

Graham, R., Jackson, M., Pilcher, R., Kilsdonk, B., 2012. Allochthonous salt in the sub-Alpine fold-thrust belt of Haute Provence, France. Salt Tectonics, Sediments Prospect. 363, 595–615. https://doi.org/10.1144/SP363.30

Gunay, G., 2002. Gypsum karst, Sivas, Turkey. Environ. Geol. 42, 387–398. https://doi.org/DOI 10.1007/s00254-002-0532-0

Gürer, D., van Hinsbergen, D.J.J., Matenco, L., Corfu, F., Cascella, A., 2016. Kinematics of a former oceanic plate of the Neotethys revealed by deformation in the Ulukisla basin (Turkey). Tectonics 35, 2385–2416. https://doi.org/10.1002/2016TC004206

Hardie, L.A., Eugster, H.P., 1971. The depositional environment of marine evaporites: a case for shallow clastic accumulation. Sedimentology 16, 187–220. https://doi.org/10.1111/j.1365-3091.1971.tb00228.x

Hodgson, N.A., Farnsworth, J., Fraser, A.J., 1992. Salt-related tectonics, sedimentation and hydrocarbon plays in the Central Graben, North Sea, UKCS. Geol. Soc. London, Spec. Publ. 67, 31–63. https://doi.org/10.1144/GSL.SP.1992.067.01.03

Hudec, M., Jackson, M.P.A., 2017. Salt Tectonics: Principles and Practice. Press, Cambridge University.

Hudec, M.R., 1992. The Onion Creek salt diapir.pdf, in: Hardman, R.F.P. (Ed.), Exploration Britain: Geological Insights for the Next Decade. Geological Society of London Special Publication 67, pp. 31–63.

Hudec, M.R., Jackson, M.P. a, 2007. Terra infirma: Understanding salt tectonics. Earth-Science Rev. 82, 1–28. https://doi.org/10.1016/j.earscirev.2007.01.001

Hudec, M.R., Jackson, M.P. a, Schultz-Ela, D.D., 2009. The paradox of minibasin subsidence into salt: Clues to the evolution of crustal basins. Bull. Geol. Soc. Am. 121, 201–221. https://doi.org/10.1130/B26275.1

Hussain, M., Warren, J.K., 1989. Nodular and enterolithic gypsum: the “sabkha-tization” of Salt Flat playa, west Texas. Sediment. Geol. 64, 13–24. https://doi.org/10.1016/0037-0738(89)90081-X

Jackson, C.A.L., Jackson, M.P.A., Hudec, M.R., Rodriguez, C.R., 2015. Enigmatic structures within salt walls of the Santos Basin-Part 1: Geometry and kinematics from 3D seismic reflection and well data. J. Struct. Geol. 75, 135–162. https://doi.org/10.1016/j.jsg.2015.01.010

Jackson, M., Pachell, M., Burg, G., Whittaker, R., 2013. Salt-encased primary minibasins in the Pre-Caspian Basin: First look at a new play, in: Applied Geodynamics Laboratory Conference 32.16. Austin, Texas.

Jackson, M.P. a, Talbot, C.J., 1986. External shapes, strain rates, and dynamics of salt structures. Geol. Soc. Am. Bull. 97, 305–323.

Kaçaroğlu, F., Değirmenci, M., Cerit, O., 2001. Water quality problems of a gypsiferous watershed: Upper Kizilirmak basin, Sivas, Turkey. Water. Air. Soil Pollut. 128, 161–180.

Kasprzyk, A., 2003. Sedimentological and diagenetic patterns of anhydrite deposits in the Badenian evaporite basin of the Carpathian Foredeep, southern Poland. Sediment. Geol. 158, 167–194. https://doi.org/http://dx.doi.org/10.1016/S0037-0738(02)00265-8

Kergaravat, C., 2016. Dynamique de formation et de déformation de mini-bassins en contexte compressif : Approche terrain, implications structurales multi-échelles et réservoirs (exemple du bassin de Sivas, Turquie). Ph.D. Thesis. Université de Pau et des Pays de l’Adour, Pau, France.

Kergaravat, C., Ribes, C., Callot, J.-P., Legeay, E., Ringenbach, J.-C., 2016. Minibasins and salt canopies in foreland fold-and-thrust belts: The central Sivas Basin, Turkey. Tectonics 35, 1–57. https://doi.org/10.1002/2016TC004186

Kergaravat, C., Ribes, C., Callot, J., Ringenbach, J., 2017. Tectono-stratigraphic evolution of salt-controlled minibasins in a fold and thrust belt, the Oligo-Miocene central Sivas basin. Struct. Geol.

Kirkham, A., 2011. Halite, sulphates, sabkha and salinas of the coastal regions and Sabkha Matti of Abu Dhabi, United Arab Emirates. Spec. Publ. Int. Assoc. Sedimentol. 43, 265–276.

Kluth, C.F., Du Chene, H.R., 2009. Late Pennsylvanian and Early Permian structural geology and tectonic history of the Paradox Basin and Uncompahgre Uplift, Colorado and Utah, in: Houston, W.S., Wray, L.L., Moreland, P.G. (Eds.), The Paradox Basin Revisited – New Developments in Petroleum Systems and Basin Analysis : RMAG 2009 Special Publication – The Paradox Basin. pp. 178–197.

Kurtman, F., 1973. Geologic and tectonic structure of the Sivas—Hafik—Zara and Imranli Region. Bull. Miner. Res. Explor. (Ankara, Turkey) 80, 1–32.

Lawton, T.F., Buck, B.J., 2006. Implications of diapir-derived detritus and gypsic paleosols in Lower Triassic strata near the Castle Valley salt wall, Paradox Basin, Utah. Geology 34, 885–888. https://doi.org/10.1130/G22574.1

Legeay, E., Mohn, G., Ringenbach, J.-C., Callot, J.-P., Ulianov, A., Kavak, K.Ş., 2019a. The pre-to post-obduction evolution of the Sivas ophiolite (Turkey) and implications for the pre-collisional history of Eastern Anatolia. Tectonics 38, 2114– 2141.

Legeay, E., Pichat, A., Kergaravat, C., Ribes, C., Callot, J.-P., Ringenbach, J.-C., 2019b. Geology of the Central Sivas Basin. J. Maps 15, 406–417.

Legeay, E., Ringenbach, J.-C., Kergaravat, C., Pichat, A., Mohn, G., Kavak, K.Ş., Callot, J.-P., Kavak, K.Ş., 2019c. Structure and kinematics of the Central Sivas Basin (Turkey): Salt deposition and tectonics in an evolving fold-and-thrust belt. Geol. Soc. London, Spec. Publ. 490.

Logan, B., 1987. The MacLeod evaporite basin, Western Australia: Holocene environments, sediments and geological evolution. American Association of Petroleum Geologists. https://doi.org/10.1306/M44465

López-Quirós, A., Barbier, M., Martín, J.M., Guichet, X., 2018. Sedimentology and diagenetic evolution of the Neogene 'Intermediate Sandstone Unit' in the halite deposits of the Granada Basin (SE Spain): the turning point in the change from marine to continental sedimentation. J. Iber. Geol. 44, 513–537. https://doi.org/10.1007/s41513-018-0069-z

Madof, A.S., Christie-Blick, N., Anders, M.H., 2009. Stratigraphic controls on a salt-withdrawal intraslope minibasin, north-central Green Canyon, Gulf of Mexico: Implications for misinterpreting sea level change. Am. Assoc. Pet. Geol. Bull. 93, 535–561. https://doi.org/10.1306/12220808082

Magee, J.W., 1991. Late Quaternary lacustrine , groundwater, aeolian and pedogenic gypsum in the Prungle Lakes , southeastern Australia. Palaeogeogr. Palaeoclimatol. Palaeoecol. 84, 3–42. https://doi.org/10.1016/0031-0182(91)90033-N

Meijers, M.J.M., Kaymakci, N., van Hinsbergen, D.J.J., Langereis, C.G., Stephenson, R. a., Hippolyte, J.-C., 2010. Late Cretaceous to Paleocene oroclinal bending in the central Pontides (Turkey). Tectonics 29, n/a-n/a. https://doi.org/10.1029/2009TC002620

Murray, R., 1964. Origin and diagenesis of gypsum and anhydrite. J. Sediment. Res. 34, 512–523.

Ocakoğlu, F., Yavuz, N., Aydın, A., Yılmaz, İ.Ö., 2017. Orbitally-driven Mid-Burdigalian Coastal Sabkha cycles from the Sivas Basin: Sedimentological, paleontological, and geochemical data. Palaeogeogr. Palaeoclimatol. Palaeoecol. in press. https://doi.org/10.1016/j.palaeo.2017.11.035

Okay, A.I., Tüysüz, O., Satir, M., Ozcan-Altiner, S., Altiner, D., Sherlock, S., Eren, R.H., 2006. Cretaceous and Triassic subduction-accretion, high-pressure–low-temperature metamorphism, and continental growth in the Central Pontides, Turkey. Geol. Soc. Am. Bull. 118, 1247–1269.

Oluboyo, A., Gawthorpe, R., Bakke, K., Hadler-Jacobsen, F., 2014. Salt tectonic controls on deep-water turbidite depositional systems: Miocene, southwestern Lower Congo Basin, offshore Angola. Basin Res. 26, 597–620.

Ortí, F., 2011. Selenite facies in marine evaporites: a review. Spec. Publ. Int. Assoc. Sedimentol. 43, 431–464.

Özçelik, O., Altunsoy, M., 1996. Clastic petrofacies, provenance and organic facies of the Bozbel Formation (Lutetian) in the Eastern Sivas Basin (Turkey). Mar. Pet. Geol. 13, 493–501. https://doi.org/10.1016/0264-8172(96)00006-2

Pichat, A., 2017. Dynamique des systèmes évaporitiques d'un bassin d'avant-pays salifère et processus diagénétiques associés au contexte halocinétique : exemple du bassin de Sivas en Turquie. PhD. Thesis. Université de Pau et des Pays de l'Adour, France.

Pichat, A., Hoareau, G., Callot, J.-P., Legeay, E., Kavak, K.S., Révillon, S., Parat, C., Ringenbach, J.-C., 2018. Evidence of multiple evaporite recycling processes in a salt-tectonic context, Sivas Basin, Turkey. Terra Nov. 30, 40–49. https://doi.org/10.1111/ter.12306

Pichat, A., Hoareau, G., Callot, J.P., Ringenbach, J.C., 2016. Diagenesis of Oligocene continental sandstones in salt-walled mini-basins-Sivas Basin, Turkey. Sediment. Geol. 339, 13–31. https://doi.org/10.1016/j.sedgeo.2016.03.025

Pilcher, R.S., Blumstein, R.D., 2007. Brine volume and salt dissolution rates in Orca Basin, northeast Gulf of Mexico. Am. Assoc. Pet. Geol. Bull. 91, 823–833. https://doi.org/10.1306/12180606049

Poisson, A., Berger, J.-P., Kangal, Ö., Kavak, K., Temiz, H., Vrielynck, B., 2012. Stratigraphic studies in the Sivas Basin, the role of the charophytes (central Anatolia, Turkey)., in: 10th Swiss Geoscience Meeting. Bern, Swiss, p. 204.

Poisson, A., Guezou, J.-C., Ozturk, A., Inan, S., Temiz, H., Gürsoy, H., Kavak, K., Özden, S., 1996. Tectonic setting and evolution of the Sivas Basin, Central Anatolia, Turkey. Int. Geol. Rev. 38, 838–853. https://doi.org/10.1080/00206819709465366

Poisson, A., Orszag-sperber, F., Temiz, H., 2010. Stratigraphic and polyphased tectonic evolution of the Sivas Basin (Central Anatolia, Turkey). Darius Annu. Rep. 2010 - Propos. No Wd 09-11 1–48.

Poprawski, Y., Basile, C., Agirrezabala, L., Jaillard, E., Gaudin, M., Jacquin, T., 2014. Sedimentary and structural record of the Albian growth of the Bakio salt diapir (the Basque Country, northern Spain). Basin Res. 26, 746–766. https://doi.org/10.1111/bre.12062

Poprawski, Y., Basile, C., Jaillard, E., Gaudin, M., Lopez, M., 2016. Halokinetic sequences in carbonate systems: An example from the Middle Albian Bakio Breccias Formation (Basque Country, Spain). Sediment. Geol. 334, 34–52. https://doi.org/10.1016/j.sedgeo.2016.01.013

Prather, B., 2000. Calibration and visualization of depositional process models for above-grade slopes: a case study from the Gulf of Mexico. Mar. Pet. Geol. 17, 619–638.

Quirk, D.G., Schødt, N., Lassen, B., Ings, S.J., Hsu, D., Hirsch, K.K., Nicolai, C. Von, Quirk, D.G., Schødt, N., Lassen, B., Ings, S.J., 2012. Salt tectonics on passive margins: examples from Santos, Campos and Kwanza basins. Geol. Soc. London, Spec. Publ. 363, 207–244. https://doi.org/10.1144/SP363.10

Raup, O.B., Hite, R.J., 1992. Lithology of evaporite cycles and cycle boundaries in the upper part of the Paradox Formation of the Hermosa Group of Pennsylvanian age in the Paradox Basin, Utah and Colorado. U.S. Geol. Surv. Bull. 2000-B 37.

Ribes, C., 2015. Interaction entre la tectonique salifère et la sédimentation dans des mini-bassins : Exemple de l'Oligo- Miocène du bassin de Sivas, Turquie. Ph.D. Thesis. Université de Pau et des Pays de l'Adour, France.

Ribes, C., Kergaravat, C., Bonnel, C., Crumeyrolle, P., Callot, J.P., Poisson, A., Temiz, H., Ringenbach, J.C., 2015. Fluvial sedimentation in a salt-controlled mini-basin: Stratal patterns and facies assemblages, Sivas Basin, Turkey. Sedimentology 62, 1513–1545. https://doi.org/10.1111/sed.12195

Ribes, C., Kergaravat, C., Crumeyrolle, P., Lopez, M., Bonnel, C., Poisson, A., Kavak, K.S., Callot, J.P., Ringenbach, J.C., 2016. Factors controlling stratal pattern and facies distribution of fluvio-lacustrine sedimentation in the Sivas mini-basins, Oligocene (Turkey). Basin Res. 1–26. https://doi.org/10.1111/bre.12171

Ribes, C., Lopez, M., Kergaravat, C., Crumeyrolle, P., Poisson, A., Callot, J.-P., Paquette, J.-L., Ringenbach, J.-C., 2018. Facies partitioning and stratal pattern in salt-controlled marine to continental mini-basins: Examples from the late Oligocene to early Miocene of the Sivas Basin, Turkey. Mar. Pet. Geol. 93, 468–496.

Ringenbach, J.C., Salel, J.F., Kergaravat, C., Ribes, C., Bonnel, C., Callot, J.-P.P., 2013. Salt tectonics in the Sivas Basin, Turkey: Outstanding seismic analogues from outcrops. First Break 31, 93–101. https://doi.org/10.3997/1365-2397.2013016

Robertson, A., Parlak, O., Ustaömer, T., 2012. Overview of the Palaeozoic–Neogene evolution of Neotethys in the Eastern Mediterranean region (southern Turkey, Cyprus, Syria). Pet. Geosci. 18, 381–404. https://doi.org/10.1144/petgeo2011-091.1354-0793/12/

Rodriguez, C.R., Jackson, C.A.-L., Bell, R., Rotevatn, A., Francis, M., 2017. Submarine salt dissolution in the Santos Basin, offshore Brazil, in press. Basin Res. https://doi.org/10.31223/osf.io/en4x7

Rolland, Y., Galoyan, G., Sosson, M., Melkonyan, R., Avagyan, A., 2010. The Armenian Ophiolite: insights for Jurassic back-arc formation, Lower Cretaceous hot spot magmatism and Upper Cretaceous obduction over the South Armenian Block. Geol. Soc. London, Spec. Publ. 340, 353–382.

Roosta, H., Jalalifar, H., Nasab, S.K., Ranjbar, M., 2019. Seven years of surface deformation above the buried Nasr-Abad salt diapir using InSAR time-series analysis, Central Iran. J. Geodyn. 130, 1–11. https://doi.org/10.1016/j.jog.2019.05.006

Rouchy, J., Bernet-Rollande, M.-C., Maurin, A.-F., 1986. Pétrographie descriptive des évaporites, applications sur le terrain en subsurface et au laboratoire, in: TECHNIP(CNRS) (Ed.), Les Séries à Évaporites En Exploration Pétrolière: Methodes Géologiques, Volume 1. Chambre syndicale de la recherche et de la production du pétrole et du gaz naturel - Comité des Techniciens et GRECO 52, Paris, pp. 73–122.

Rouchy, J., Blanc-Valleron, M., 2006. Les évaporites: matériaux singuliers, milieux extrèmes. Paris.

Rowan, M.G., Giles, K.A., Hearon, T.E., Fiduk, J.C., Rowan, M.G., 2016. Megaflaps adjacent to salt diapirs. Am. Assoc. Pet. Geol. Bull. 100, 1723–1747. https://doi.org/10.1306/05241616009

Rowan, M.G., Lawton, T.F., Giles, K.A., Ratliff, R.A., 2003. Near-salt deformation in La Popa basin, Mexico, and the northern Gulf of Mexico: A general model for passive diapirism. Am. Assoc. Pet. Geol. Bull. 87, 733–756. https://doi.org/10.1306/01150302012

Schreiber, B.C., El Tabakh, M., 2000. Deposition and early alteration of evaporites. Sedimentology 47, 215–238. https://doi.org/10.1046/j.1365-3091.2000.00002.x

Shearman, D., 1978. Halite in sabkha environments. Mar. evaporites 30–42.

Stewart, S.A., Clark, J.A., 1999. Impact of salt on the structure of the Central North Sea hydrocarbon fairways, in: Fleet, A.J., Boldy, S.A.R. (Eds.), Petroleum Geology of Northwest Europe: Proceedings of the 5th Conference on the Petroleum Geology of Northwest Europe. Geological Society of London, pp. 179–200. https://doi.org/10.1144/0050179

Tekin, E., 2001. Stratigraphy, geochemistry and depositional environment of the celestine-bearing gypsiferous formations of the Tertiary Ulas-Sivas Basin, East-Central Anatolia (Turkey). Turkish J. Earth Sci. 10, 35–49.

Testa, G., Lugli, S., 2000. Gypsum-anhydrite transformations in Messinian evaporites of central Tuscany (Italy). Sediment. Geol. 130, 249–268. https://doi.org/10.1016/S0037-0738(99)00118-9

Trude, J., Graham, R., Pilcher, R., 2012. Salt-related structures on the Bristol Channel coast, Somerset (UK). Geol. Soc. London, Spec. Publ. 363, 533–544. https://doi.org/10.1144/SP363.26

van den Belt, F.J., de Boer, P.L., 2007. A shallow-basin model for 'Saline Giants' based on isostasy-driven subsidence, in: Nichols, G., Williams, E., Paola, C. (Eds.), Sedimentary Processes, Environments and Basins: A Tribute to Peter Friend. Internal Association of Sedimentologist, Special Publication, pp. 241–252. https://doi.org/10.1002/9781444304411.ch11

Vendeville, B.C., Jackson, M.P.A., 1992. The fall of diapirs during thin-skinned extension. Mar. Pet. Geol. 9, 354–371. https://doi.org/10.1016/0264-8172(92)90047-I

Volozh, Y., Talbot, C., Ismail-Zadeh, A., 2003. Salt structures and hydrocarbons in the Pricaspian basin. Am. Assoc. Pet. Geol. Bull. 87, 313–334. https://doi.org/10.1306/09060200896

Warren, J., 1991. Sulfate dominated sea-marginal and platform evaporative settings: Sabkhas and salinas, mudflats and salterns. Dev. Sedimentol. 50, 69–187.

Warren, J.K., 2016. Evaporites: A Geological Compendium. Springer International Publishing.

Warren, J.K., 2011. Evaporitic source rocks: mesohaline responses to cycles of "famine or feast" in layered brines. Spec. Publ. Int. Assoc. Sedimentol. 43, 45–88.

Warren, J.K., 2010. Evaporites through time: Tectonic, climatic and eustatic controls in marine and nonmarine deposits. Earth-Science Rev. 98, 217–268. https://doi.org/10.1016/j.earscirev.2009.11.004

Warren, J.K., 1982. The hydrological setting, occurrence and significance of gypsum in late Quaternary salt lakes in South Australia. Sedimentology 29, 609–637. https://doi.org/10.1111/j.1365-3091.1982.tb00071.x

Warren, J.K., Kendall, C.G.S.C., 1985a. Comparison of sequences formed in marine sabkha (subaerial) and salina (subaqueous) settings--modern and ancient. Am. Assoc. Pet. Geol. Bull. 69, 1013–1023.

Warren, J.K., Kendall, C.G.S.C., 1985b. Comparison of sequences formed in marine sabkha (subaerial) and salina (subaqueous) settings--modern and ancient. Am. Assoc. Pet. Geol. Bull. 69, 1013–1023.

Yilmaz, A., Yilmaz, H., 2006. Characteristic features and structural evolution of a post collisional basin: The Sivas Basin, Central Anatolia, Turkey. J. Asian Earth Sci. 27, 164–176. https://doi.org/10.1016/j.jseaes.2005.02.006

Zarei, M., Raeisi, E., Talbot, C.J., 2012. Karst development on a mobile substrate: Konarsiah salt extrusion, Iran. Geol. Mag. 149, 412–422. https://doi.org/10.1017/S0016756811000689

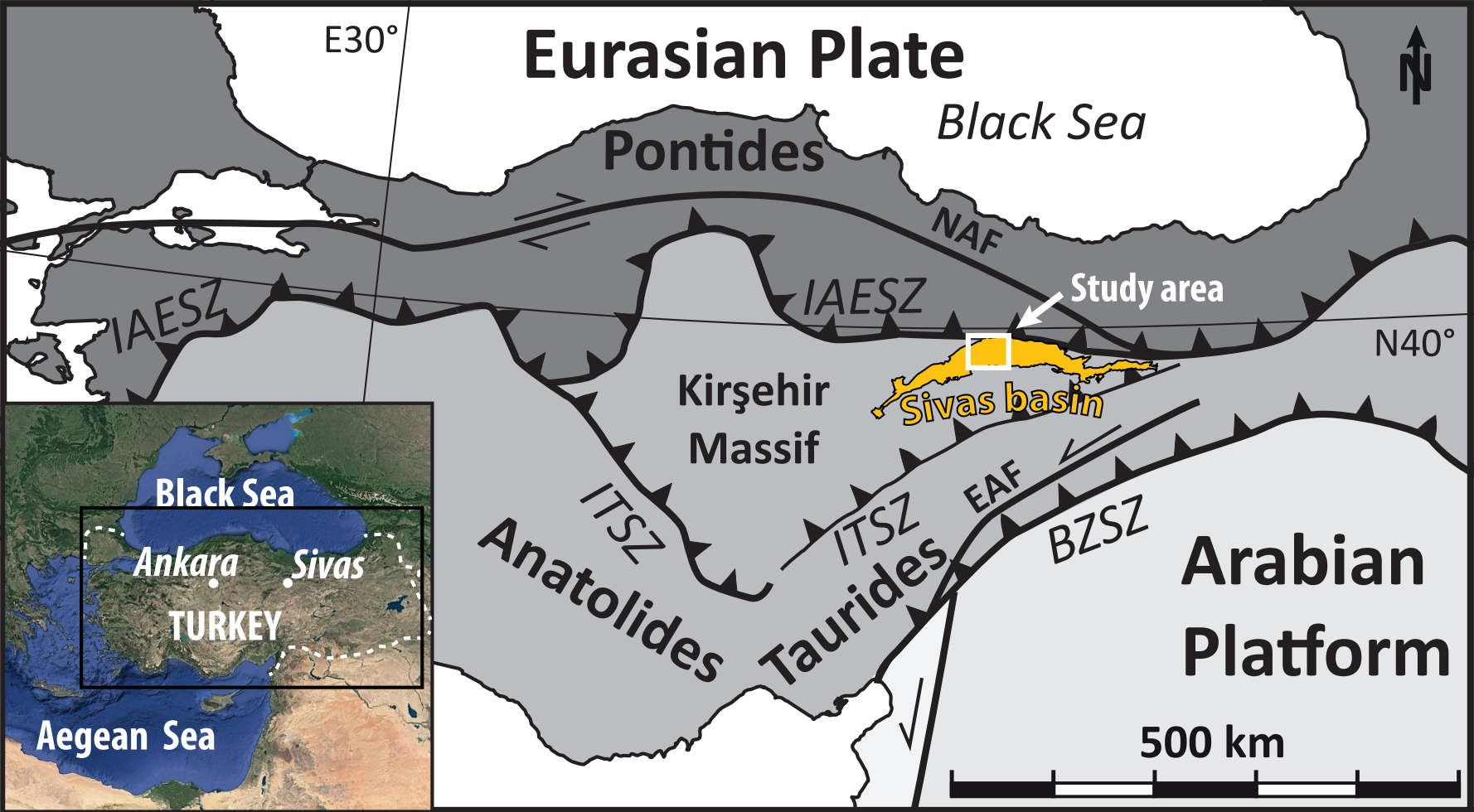
E30°
Eurasian Plate
Black Sea
Pontides
NAF
IAESZ
IAESZ
Study area
N40°
Kirşehir
Massif
Sivas basin
ITSZ
Anatolides
ITSZ
Taurides
EAF
BZSZ
Arabian
Platform
500 km
Black Sea
Ankara
Sivas
TURKEY
Aegean Sea

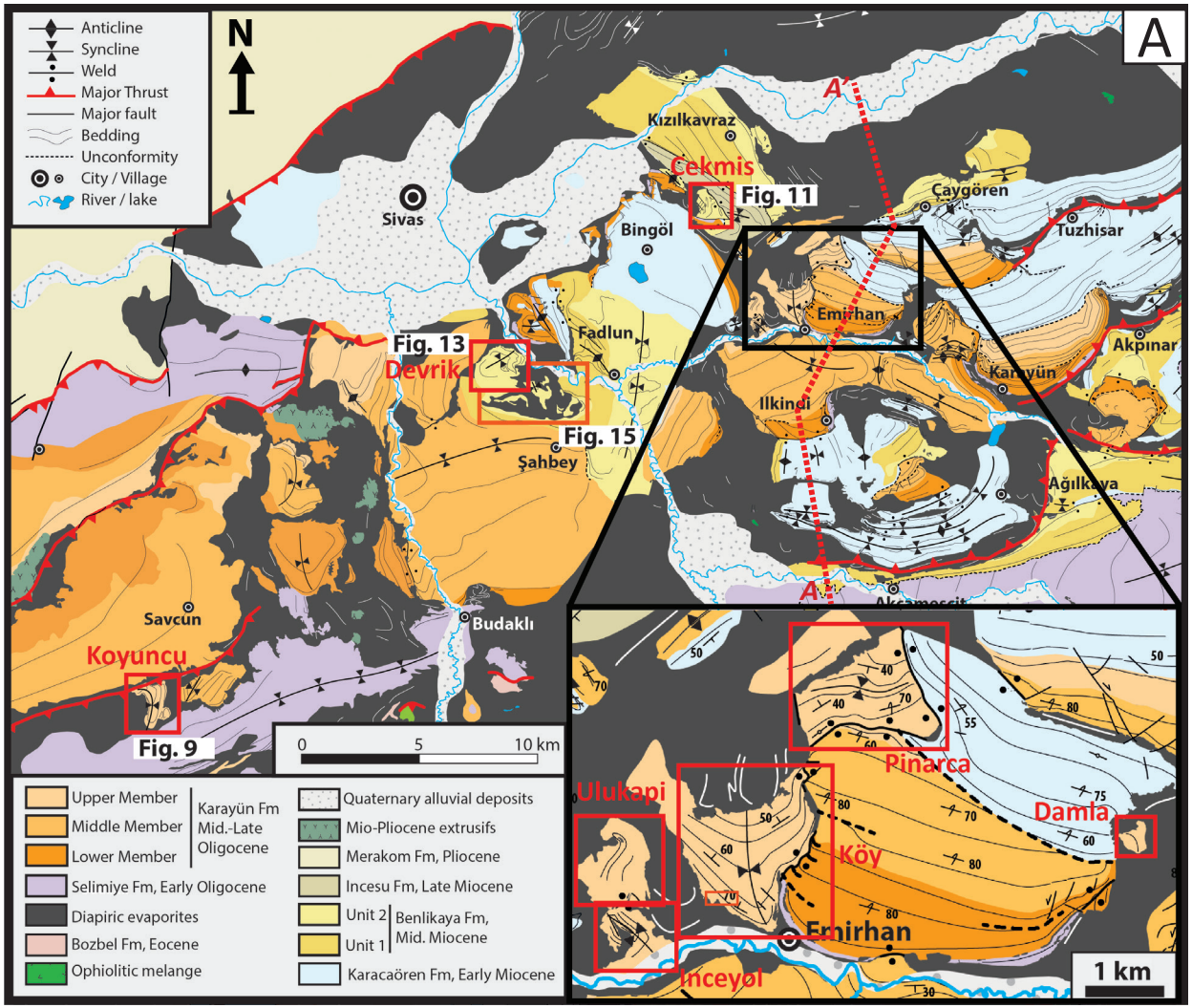

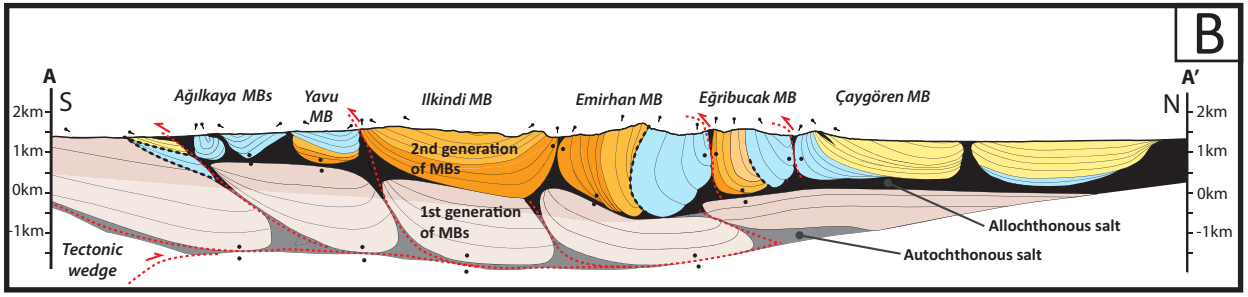

C

AGE	Ma	LITHOLOGY	FORMATIONS	DEPOSITIONAL ENVIRONMENT	THICK. (m)
QUATERNARY	2.58			Alluvium terraces and travertines	
Plio. – Piacenzian	3.600		Merakom	Lacustrine	50 to 200
Plio. – Zanclean	5.333		Incesu	Fluvial	
Miocene – Messinian	7.246				
Miocene – Tortonian	11.62		Benlikaya	**Unit 2:** Playa lake ↕ *Period of EMB formation*	500 to 1000
Miocene – Serravallian	13.82			**Unit 1:** Alluvial fan and fluvial braided	
Miocene – Langhian	15.97		Karacaören	**Unit 4:** Delta plain and restricted coastal lagon **Unit 3:** Mixed deltaïc and shallow marine carbonates **Unit 2:** Delta plain and restricted lagoon **Unit 1:** Mixed deltaïc and shallow marine carbonates	1000 to 2500
Miocene – Burdigalian	20.44				
Miocene – Aquitanian	23.03				
Oligocene – Chattian	28.1		Karayün	**Unit 3:** Fluvio-saline lacustrine ↕ *Period of EMB formation* **Unit 2:** Amalgamated fluvial braided **Unit 1:** Playa-lake with fluvial intercalations	1000 to 2500
				SALT CANOPY	?
Oligocene – Rupelian	33.9		Selimiye	Playa-lake to fluvial	1500 to 2500
Eocene – Priabonian	38.0		Tuzhisar	Marine-fed evaporites — AUTOCHTONOUS LEVEL	>200 ?
Eocene – Bartonian	41.3	Tokus	Tokus Bözbel	Shallow-water turbidites **Tokus:** nummulitic platforms (along borders) Thin-bedded turbidites with basaltic intrusions	100 to 1500
Eocene – Lutetian	47.8		Yapali	Calciturbidites	50 -100
Eocene – Ypresian	56.0	Ya	Kozluca Bahçecik	Thick-bedded turbidites and volcanoclastics Fan delta **Ya : Yagmurluseki Fm**	100 to 600
Paleo. – Thanetian	59.2		*Gazibey Fm.*	Reddish shales	100 to 2000
Paleo. – Selandian	61.6	Tecer	Ko Ce Ka Tecer	**Ce : Cercapindere** **Ko : Konakyazi** **Ka : Kaleköy** Mixed volcanoclatics, clastics and carbonate turbidites **Tecer** Shallow-water carbonate platforms	
Paleo. – Danian	66.0				
Paleo. – Maastr.	72.1				
BASEMENT – Late Cretaceous			Tauride Ophiolite	Serpentinized peridotite nappe with rare magmatic intrusions Obduction occured during Santonian-Campanian times.	3000 ?
			Ophiolitic mélange		> 50
BASEMENT – Undifferenciated Jurassic to Mid-Cretaceous			Munzur Unit	Undifferenciated platform carbonates Poorly metamorphosed	?

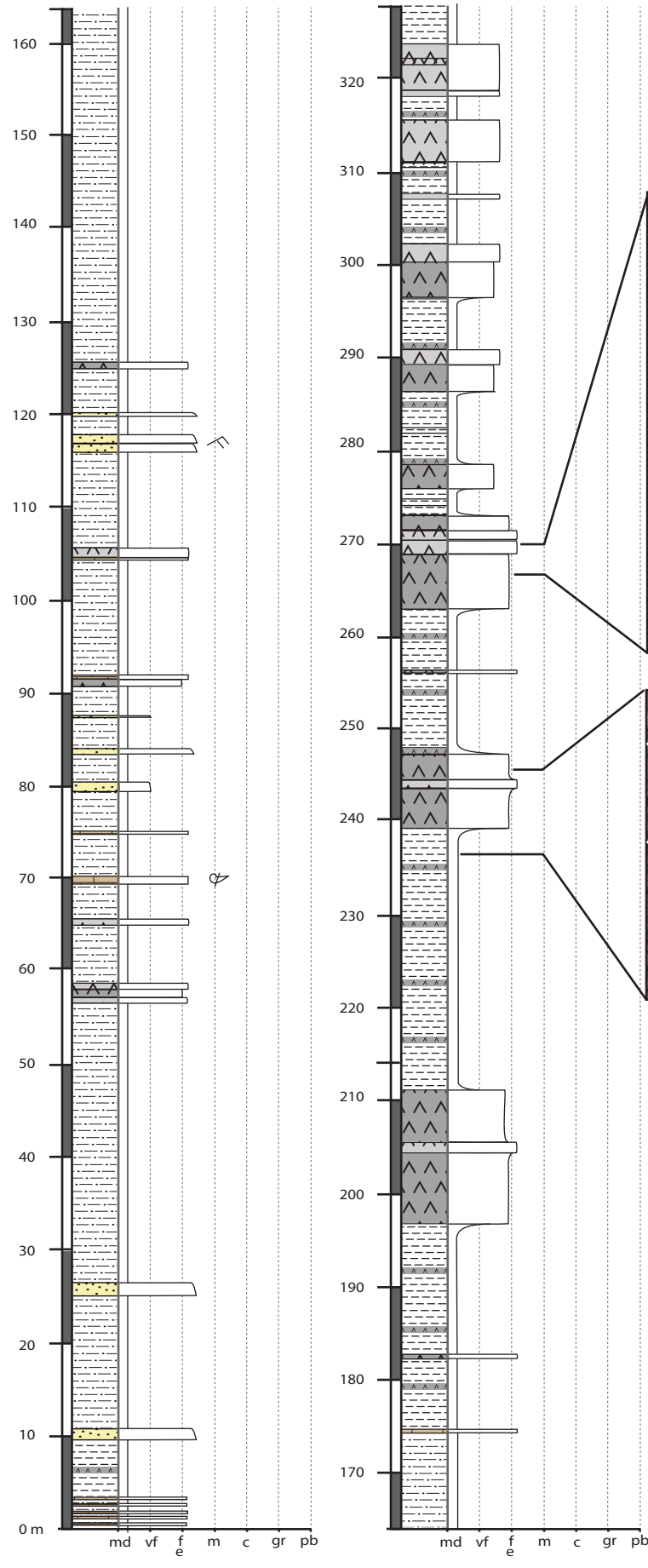

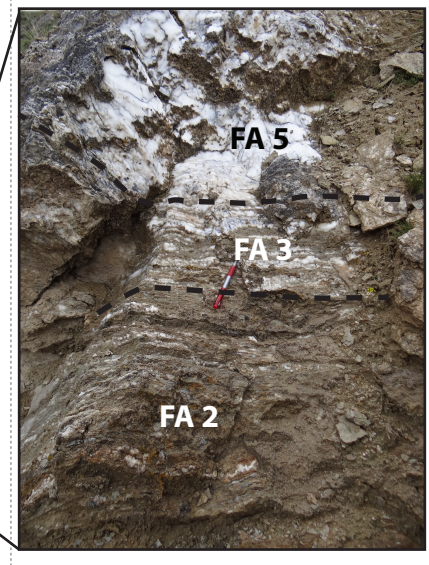

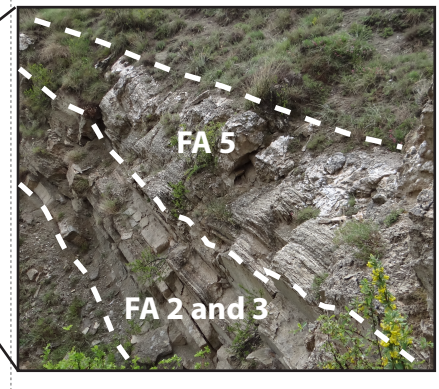

Lithologies

- Massive to nodular secondary gypsum - FA 5
- Bed alternance of laminated to nodular banded gypsum with selenite ghosts (FA 2 and 3)
- Green to red clays with sparse thin gypsum beds of FA 2
- Sandstone
- Mudstone
- Silty clays

FA 1

- Bioclasts
- Current ripples

pb: pebbles, gr: granules, c, m, f and vf: coarse, medium, fine and very fine grained sandstone, e: evaporites, md: mud

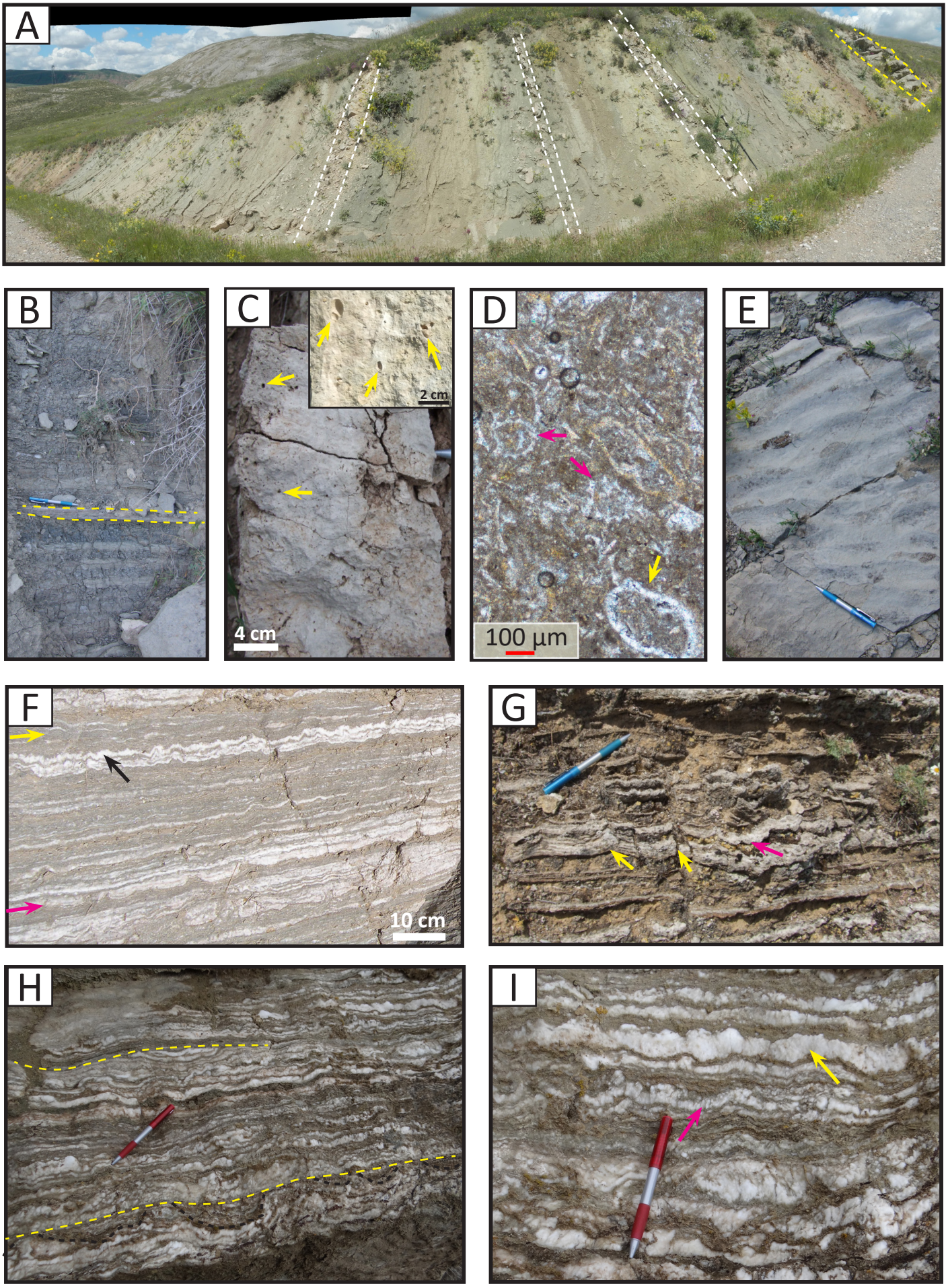
A
B
C
2 cm
4 cm
D
100 µm
E
F
10 cm
G
H
I

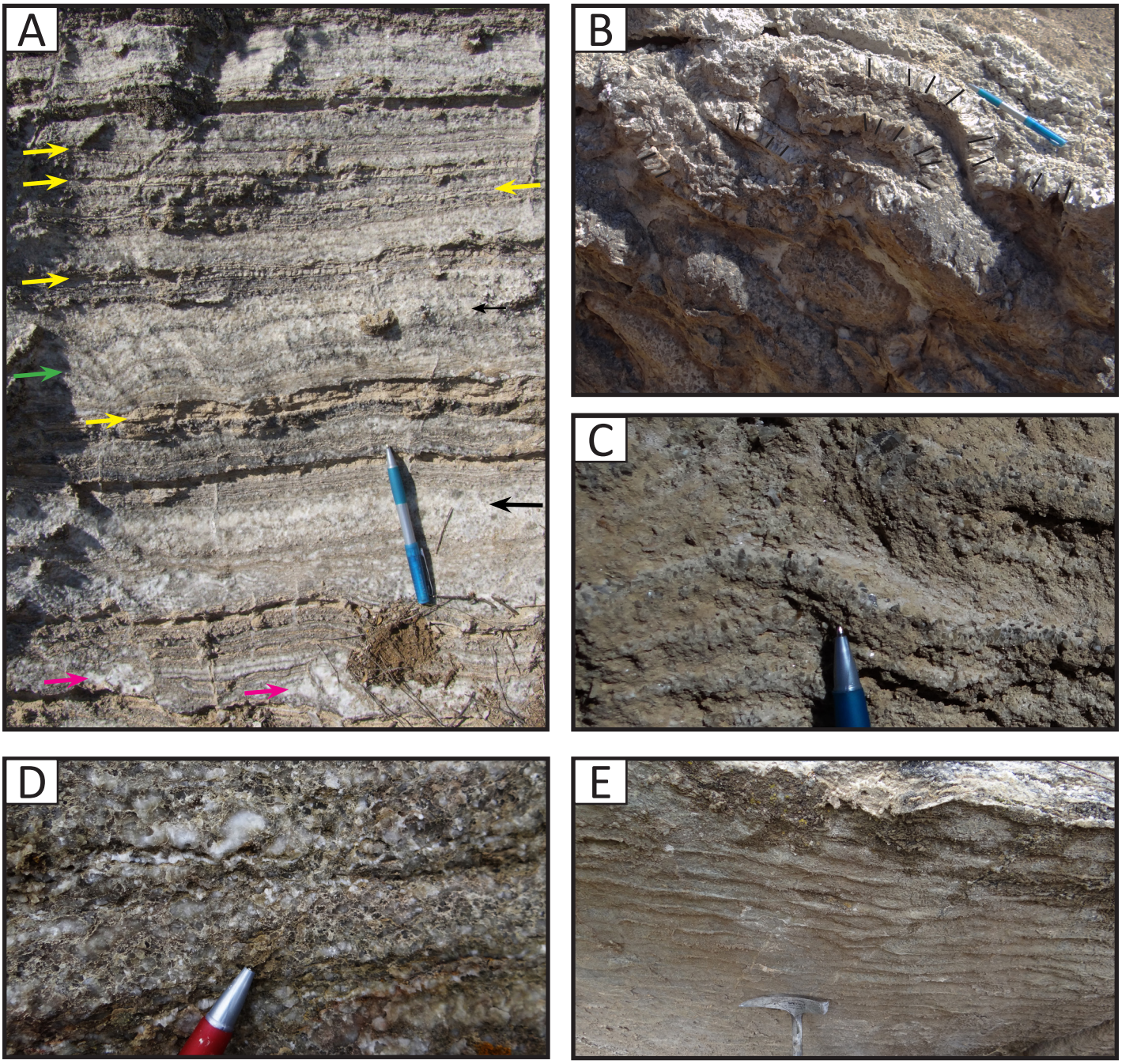
A
B
C
D
E

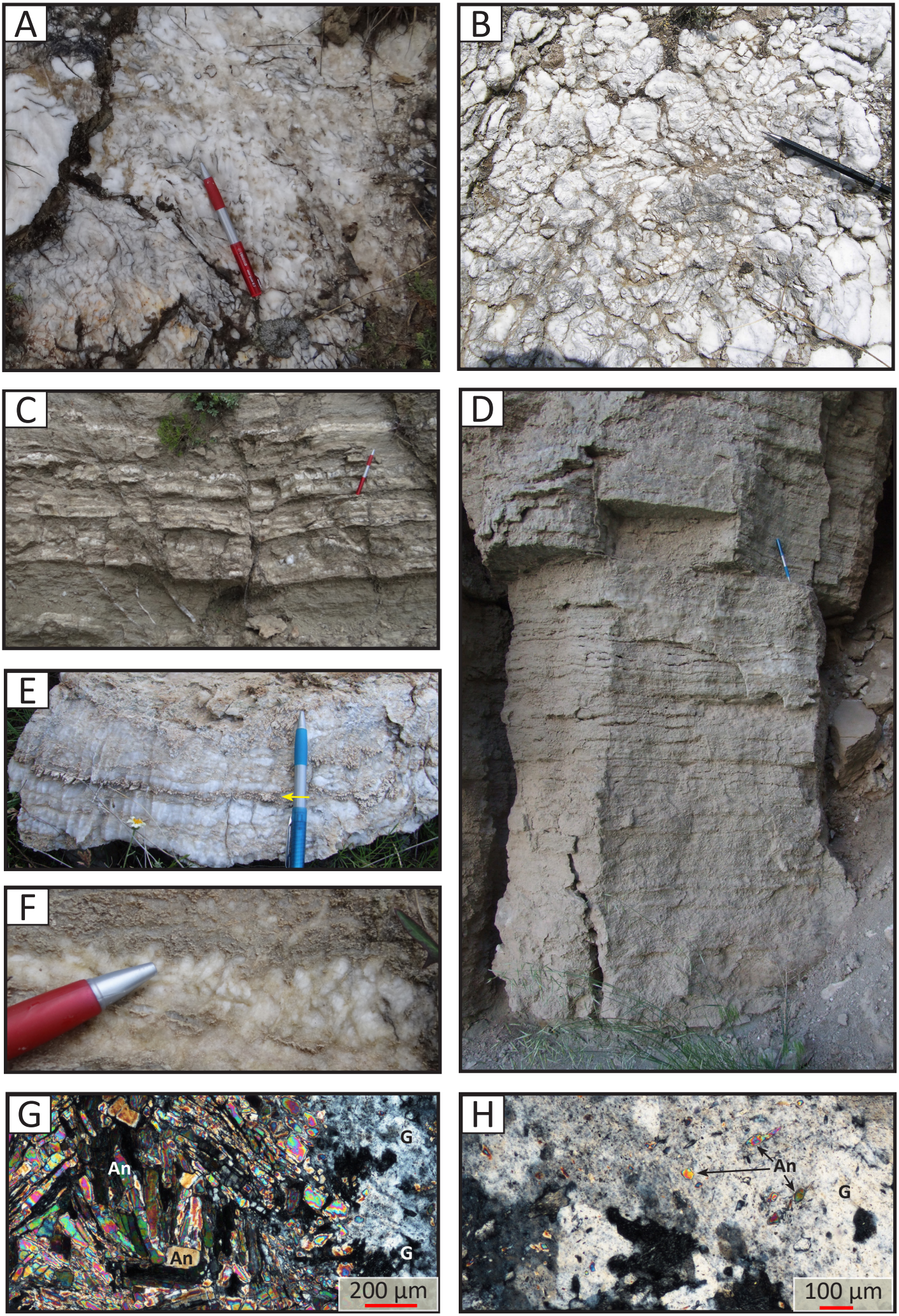
A
B
C
D
E
F
G
An
An
G
G
200 µm
H
An
G
100 µm


A


B

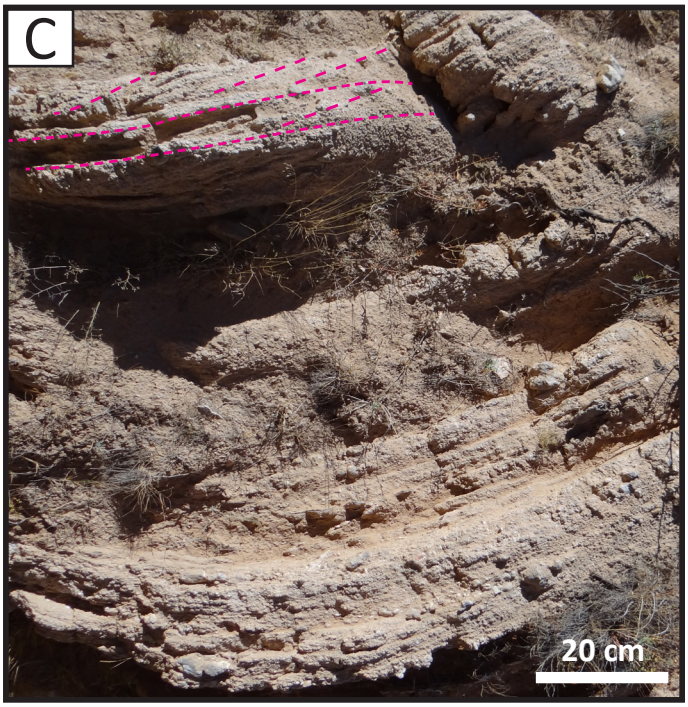
C
20 cm

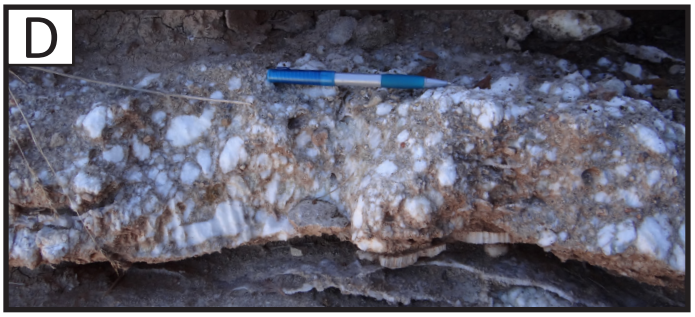
D

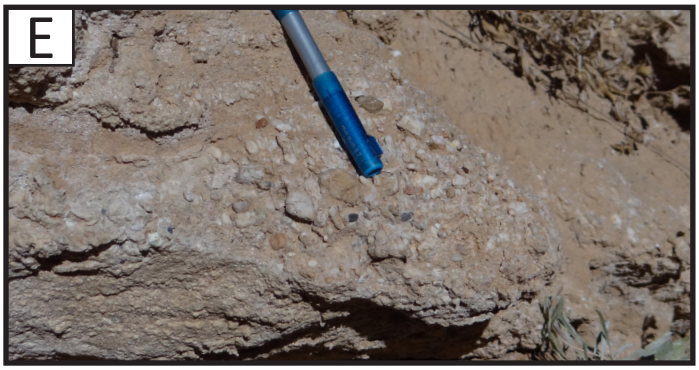
E

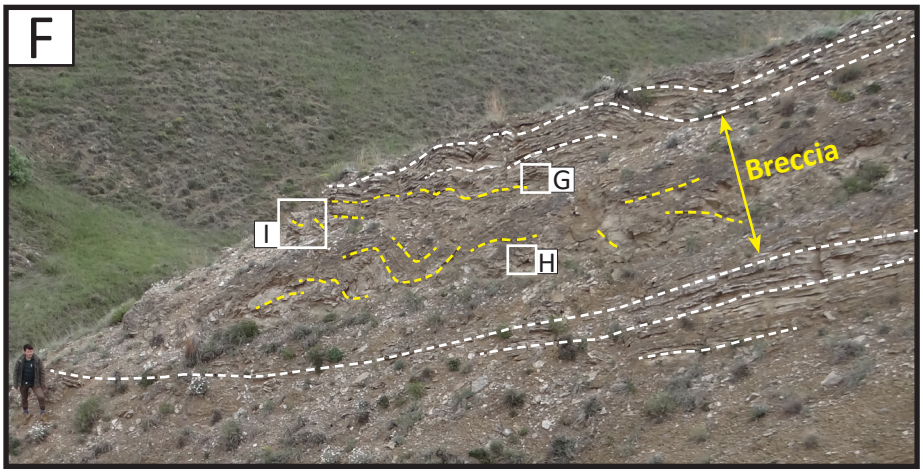
F
Breccia
G
I
H


G

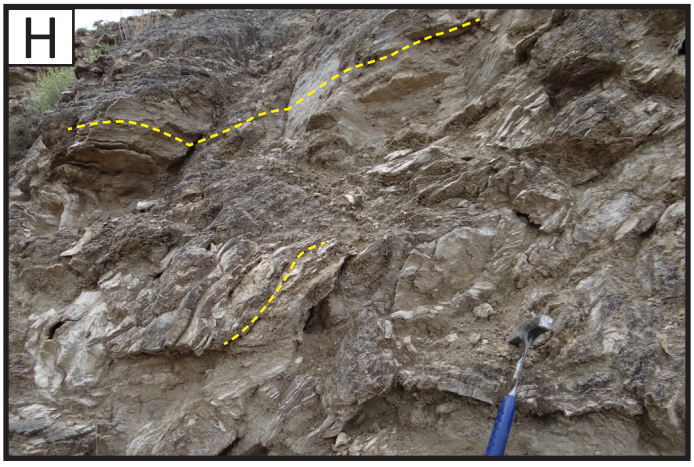
H


I

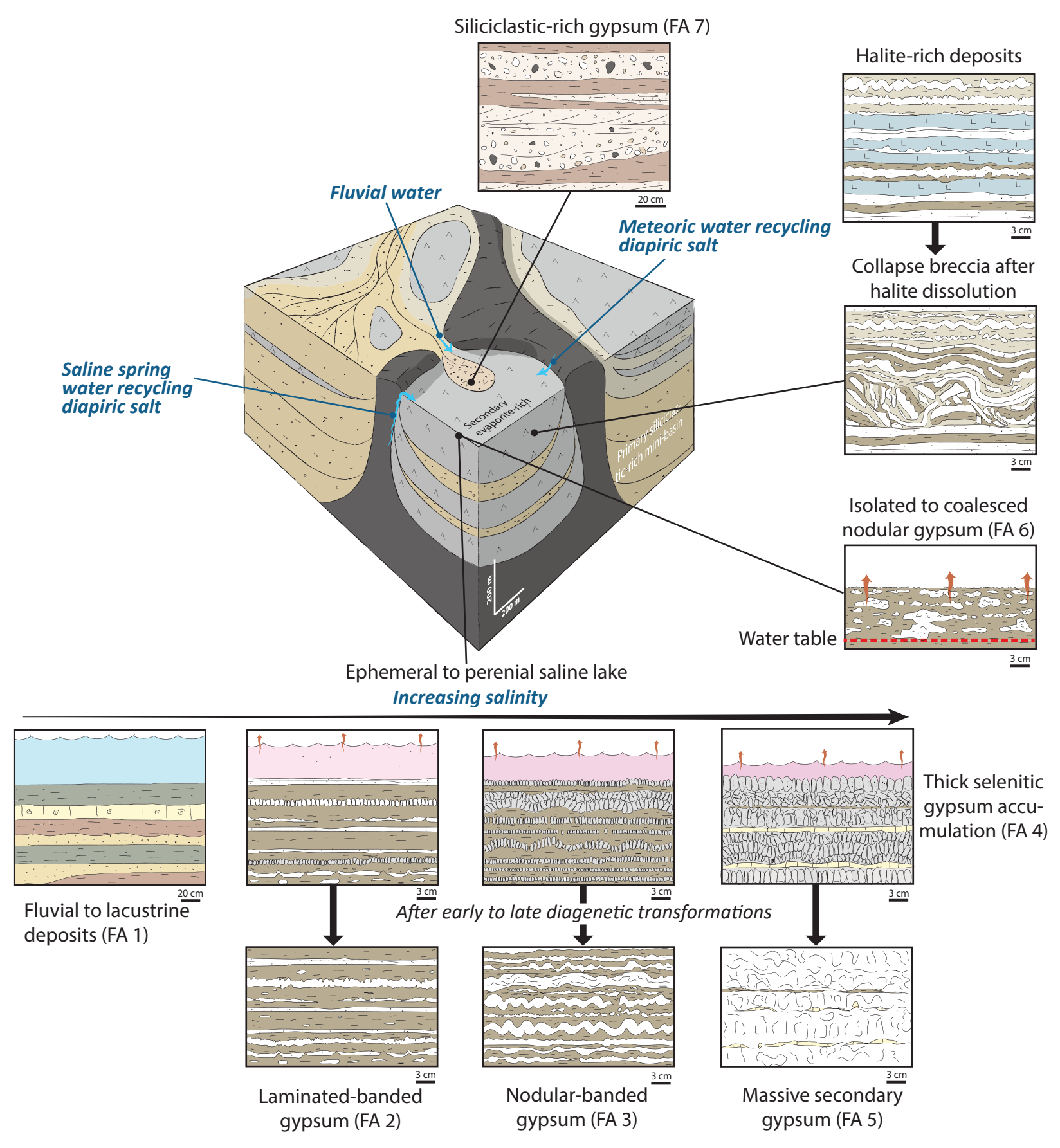
Siliciclastic-rich gypsum (FA 7)
20 cm
Halite-rich deposits
3 cm
Collapse breccia after halite dissolution
3 cm
Fluvial water
Meteoric water recycling diapiric salt
Saline spring water recycling diapiric salt
Secondary evaporite-rich
Primary siliciclastic-rich mini-basin
200 m
200 m
Isolated to coalesced nodular gypsum (FA 6)
Water table
3 cm
Ephemeral to perenial saline lake
Increasing salinity
20 cm
Fluvial to lacustrine deposits (FA 1)
3 cm
3 cm
3 cm
Thick selenitic gypsum accumulation (FA 4)
After early to late diagenetic transformations
3 cm
3 cm
3 cm
Laminated-banded gypsum (FA 2)
Nodular-banded gypsum (FA 3)
Massive secondary gypsum (FA 5)

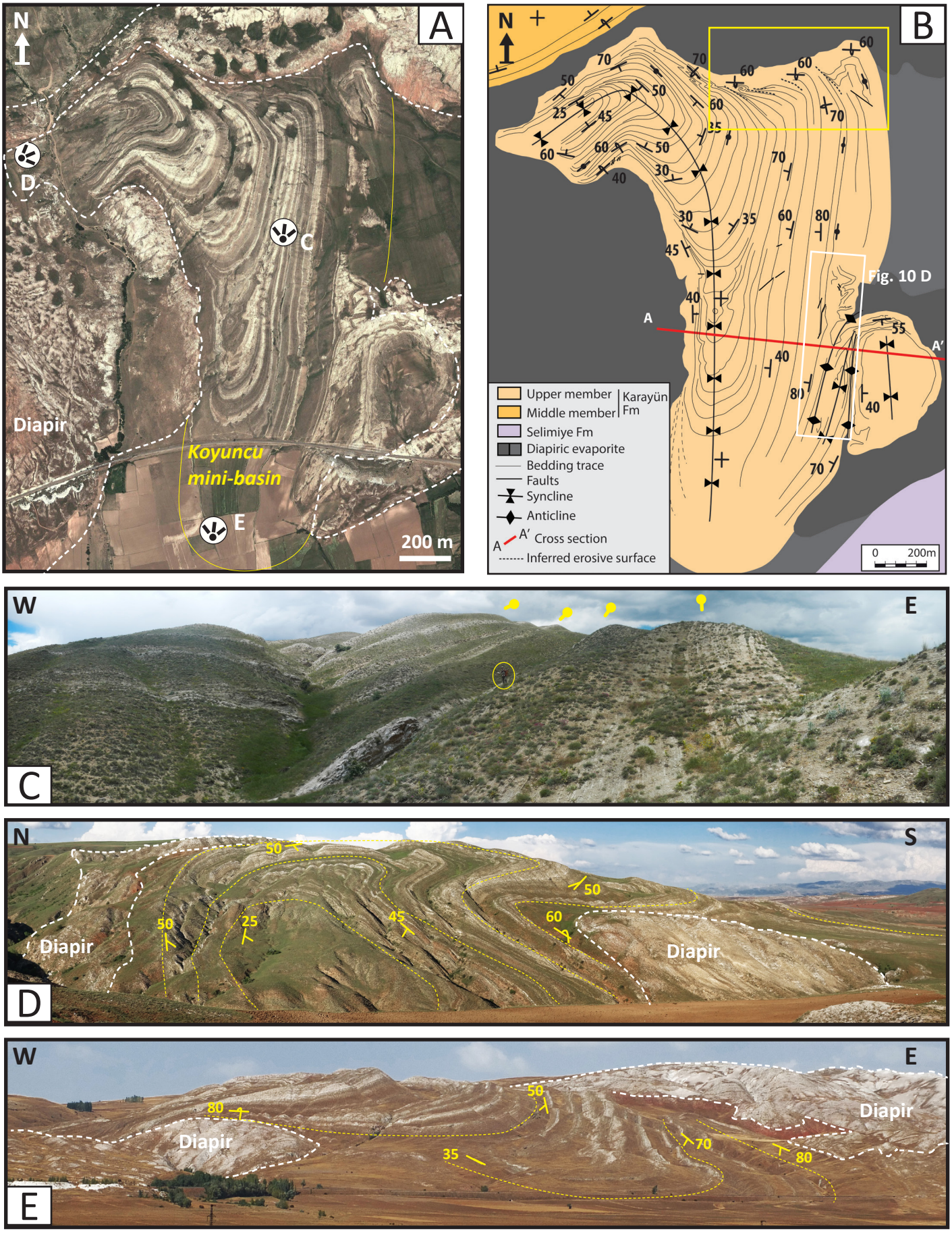
A
N
D
C
E
Diapir
Koyuncu
mini-basin
200 m
B
N
Fig. 10 D
A
A′
Upper member
Middle member
Karayün Fm
Selimiye Fm
Diapiric evaporite
Bedding trace
Faults
Syncline
Anticline
Cross section
Inferred erosive surface
0 200m
C
W
E
D
N
S
Diapir
Diapir
E
W
E
Diapir
Diapir
F
A
A′
W
E
1500m
1400m
1300m
0 200m

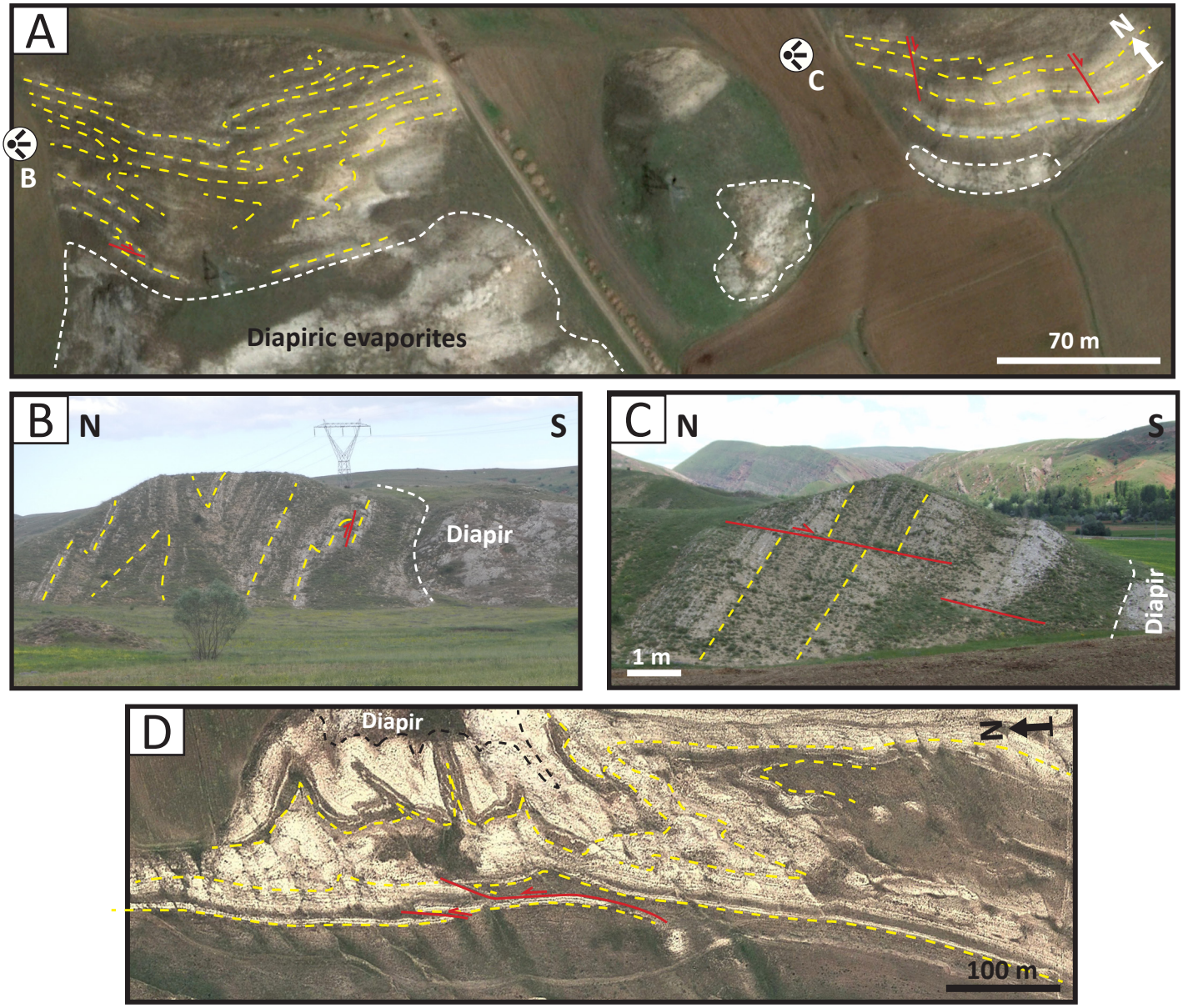
A
B
C
N
Diapiric evaporites
70 m
B
N
S
Diapir
C
N
S
Diapir
1 m
D
Diapir
N
100 m

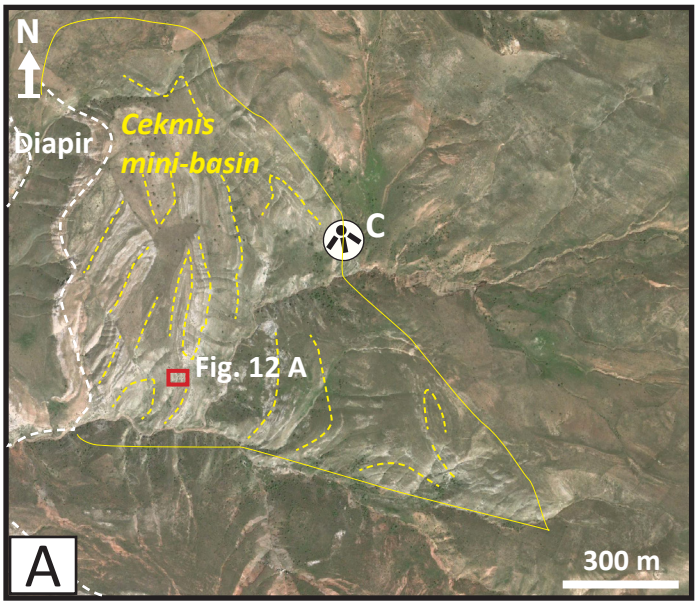
N
Diapir
Cekmis
mini-basin
C
Fig. 12 A
300 m
A

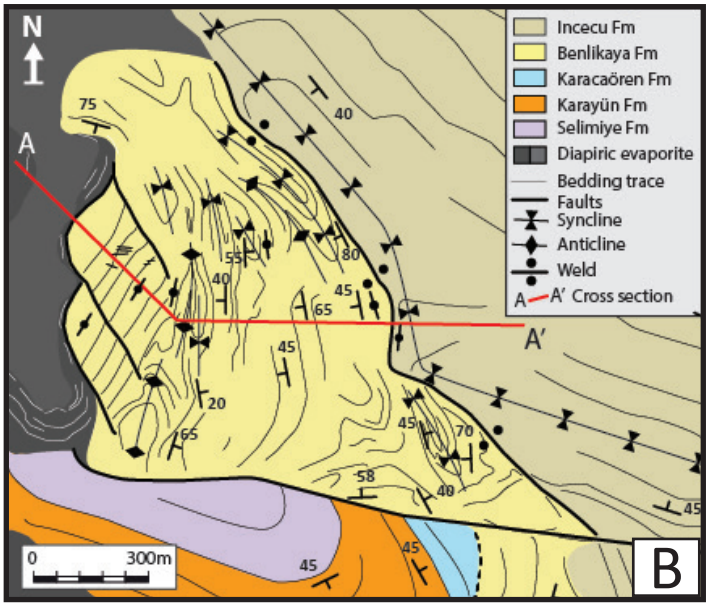
N
A
75
40
55
80
40
45
65
45
A'
45
20
65
45
70
58
40
45
45
0
300m
Incecu Fm
Benlikaya Fm
Karacaören Fm
Karayün Fm
Selimiye Fm
Diapiric evaporite
Bedding trace
Faults
Syncline
Anticline
Weld
A A' Cross section
B


E
W
5 m
C


A
NW
SE
1 m

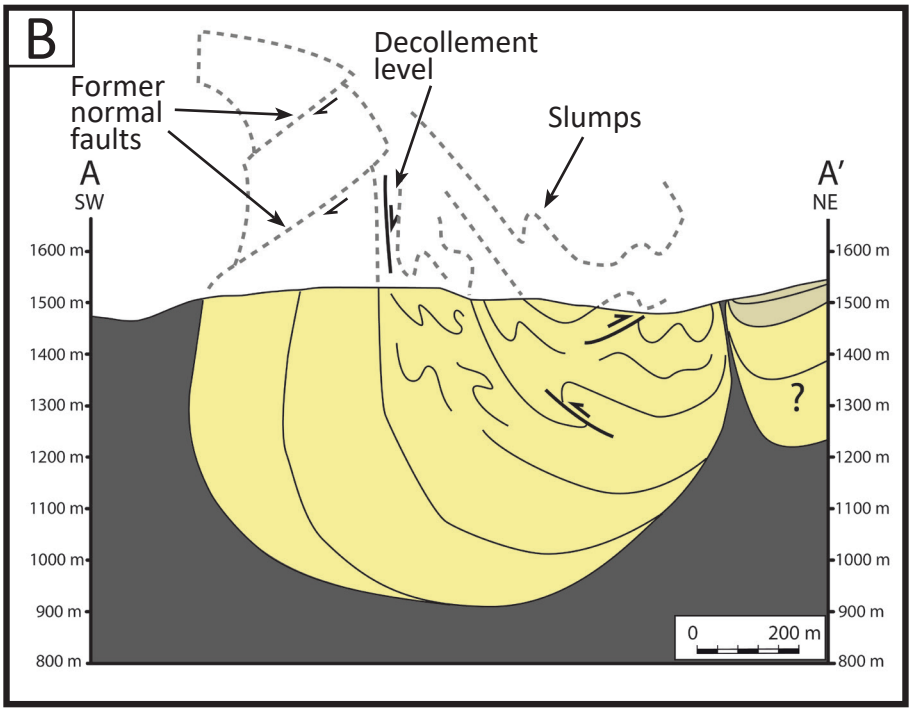
B
Former
normal
faults
Decollement
level
Slumps
A
SW
A′
NE
1600 m
1500 m
1400 m
1300 m
1200 m
1100 m
1000 m
900 m
800 m
?
0
200 m

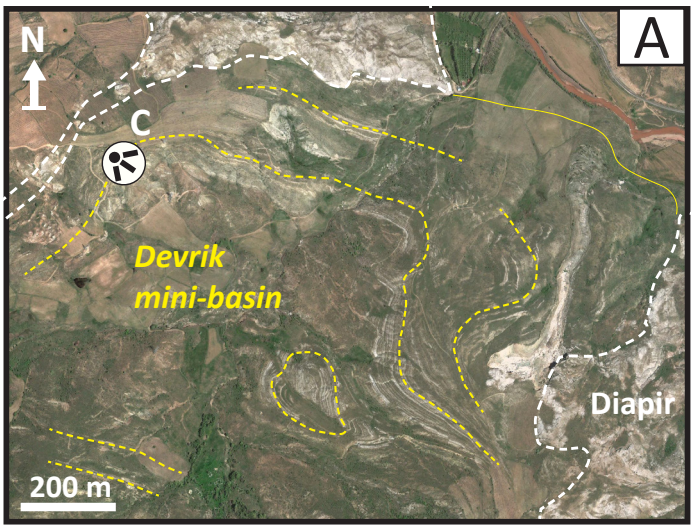
A
N
C
Devrik
mini-basin
Diapir
200 m

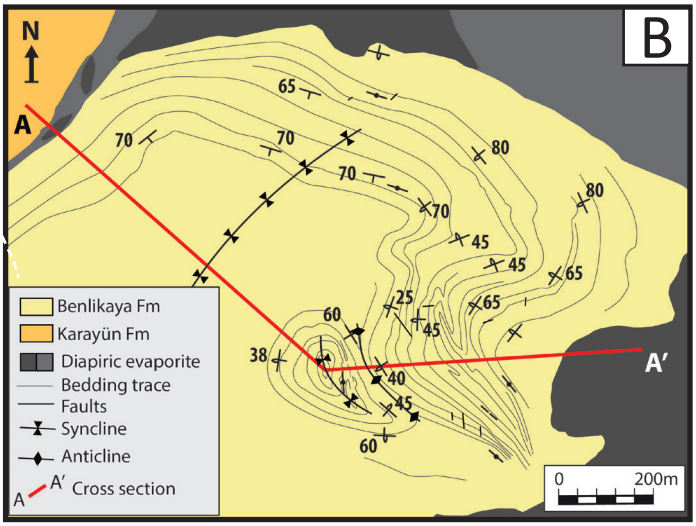
B
N
A
A′
65
70
70
70
80
80
70
45
45
65
25
65
45
60
38
40
45
60
Benlikaya Fm
Karayün Fm
Diapiric evaporite
Bedding trace
Faults
Syncline
Anticline
A A′ Cross section
0
200m

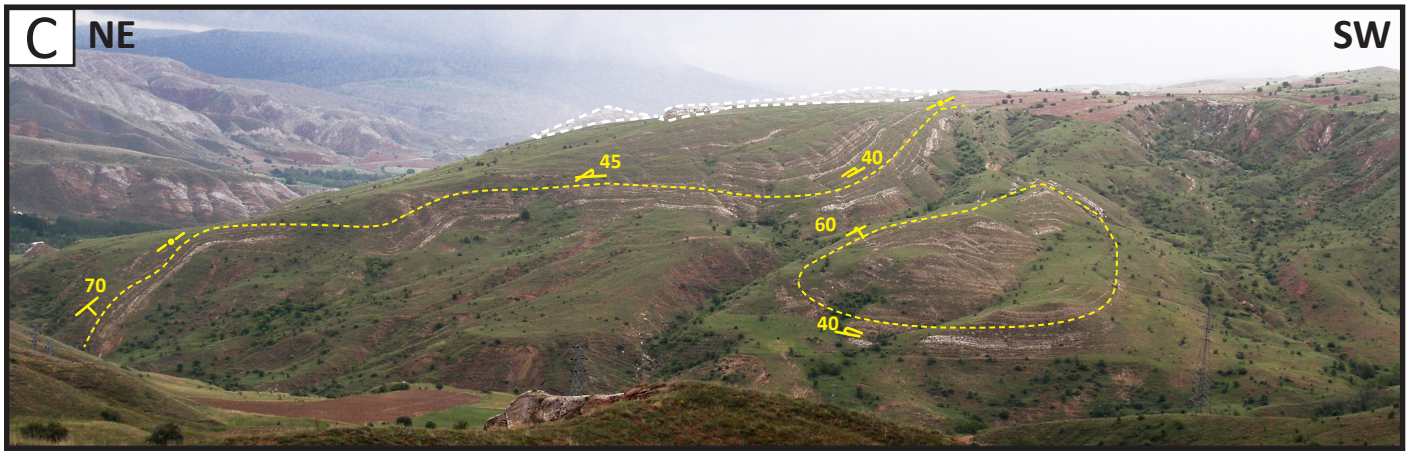
C
NE
SW
45
40
60
70
40

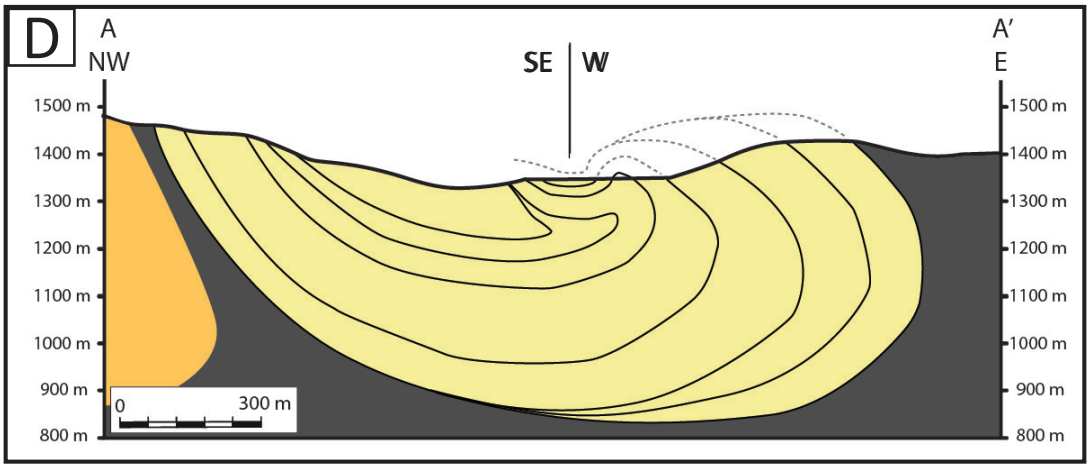
D
A
NW
SE
W
A′
E
1500 m
1400 m
1300 m
1200 m
1100 m
1000 m
900 m
800 m
0
300 m

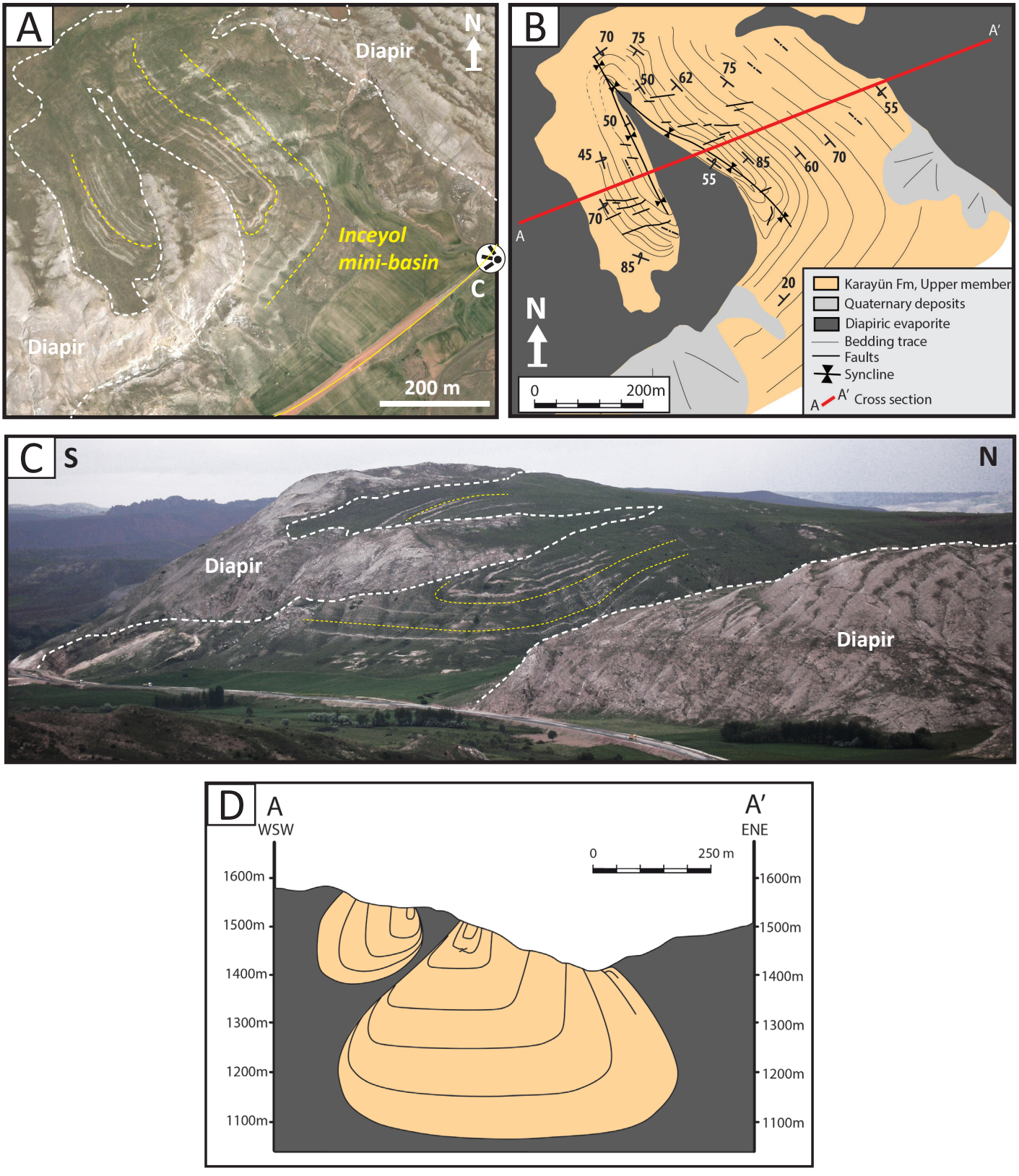
A
Diapir
N
Inceyol
mini-basin
C
Diapir
200 m
B
70
75
50
62
75
55
50
45
85
60
70
55
70
85
20
A
A′
N
0
200m
Karayün Fm, Upper member
Quaternary deposits
Diapiric evaporite
Bedding trace
Faults
Syncline
A A′ Cross section
C
S
N
Diapir
Diapir
D
A
WSW
A′
ENE
0
250 m
1600m
1500m
1400m
1300m
1200m
1100m

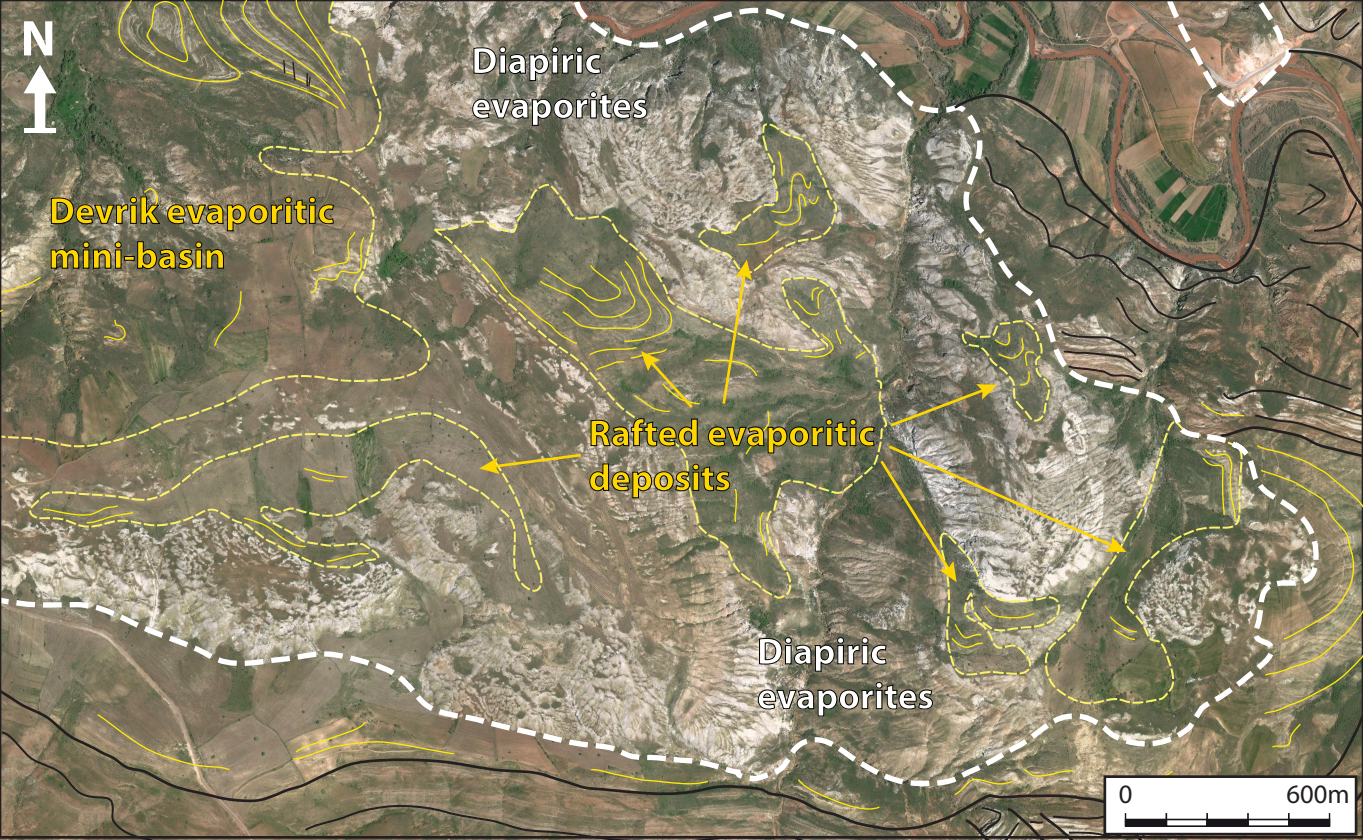
N
Diapiric evaporites
Devrik evaporitic mini-basin
Rafted evaporitic deposits
Diapiric evaporites
0
600m

A Initiation of evaporite-rich mini-basin

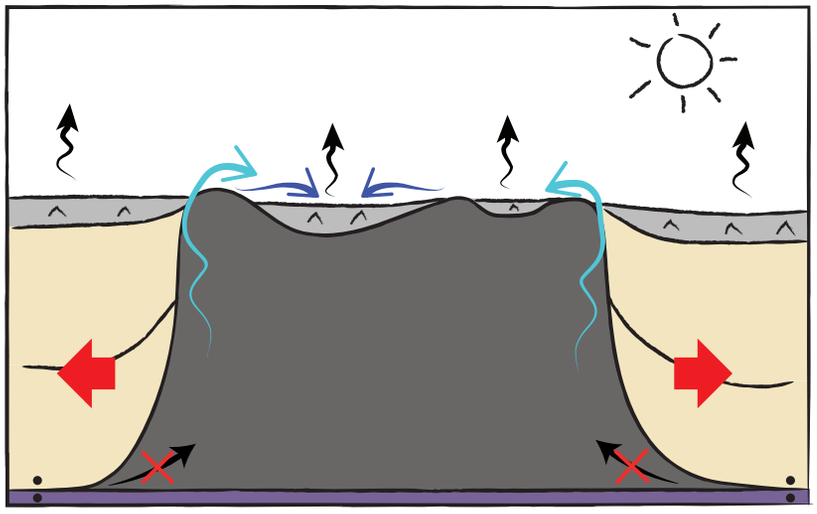

Enabled by:

- Semi-arid climate with restricted fluvial/marine inputs
- Flat topography of the diapiric stem
- Regional subsidence
- Cessation of diapir grotwh by welding of the mother salt or by extensive strains
- Fast precipitation of evaporites with dissolved salts abundantly provided by the surface and subsurface leaching of the diapiric structures

B Evaporite-rich mini-basin subsidence

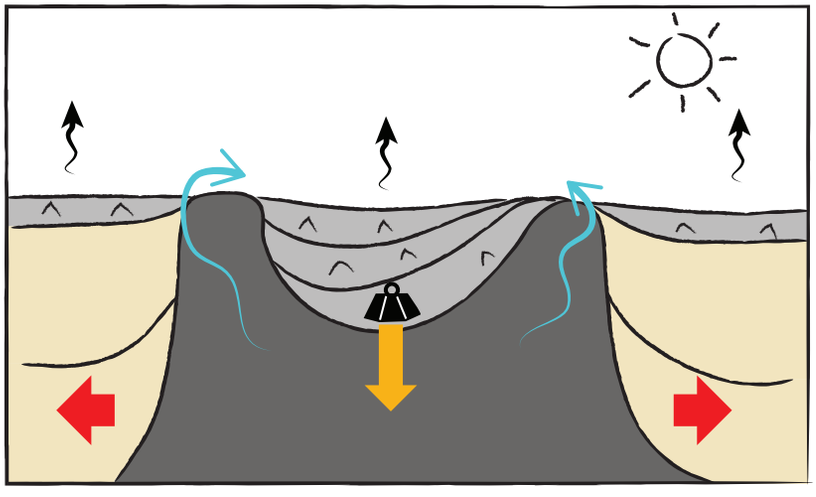

Triggered by:

- Subsurface diapir dissolution
-High density of depositional gypsum / anhydrite compared to diapiric halite
- Local transtensive strains

C Evaporite-rich mini-basin deformation

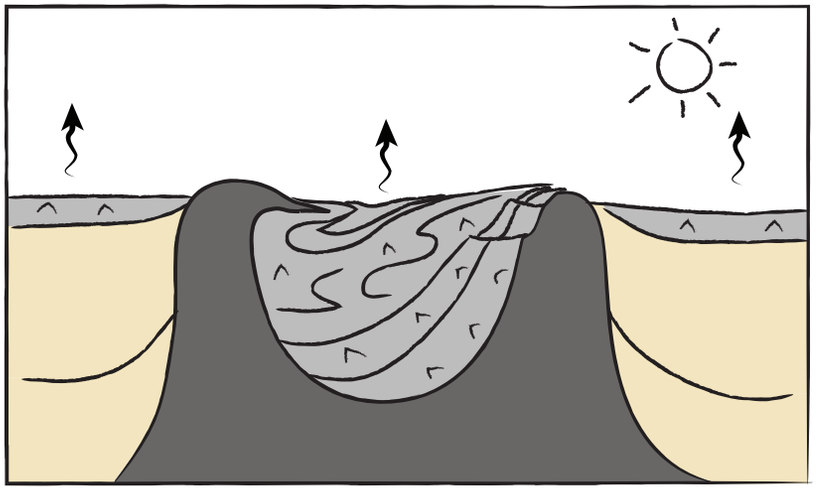

Weak rheology of evaporitic overburden allowing an encased morphology and numerous internal deformations